# 1290

## UNIVERSIDADE Ð COIMBRA

Joel Cardoso Loureiro

# NUMERICAL STUDY FOR THE OPTIMIZATION OF AN INNOVATIVE PERSONAL PROTECTIVE DEVICE

# Numerical study for the optimization of an innovative personal protective device

A dissertation submitted in partial fulfilment of the requirements for the degree of Master in Mechanical Engineering in the speciality of Energy and Environment

# Estudo numérico para a otimização de um dispositivo de proteção individual inovador

**Author**

**Joel Cardoso Loureiro**

**Advisors**

**José Joaquim da Costa**
**Nuno Cláudio Ferreira Rosa**

**Committee**

| | |
|---|---|
| Chair | Professor Doutor **Adélio Manuel Rodrigues Gaspar** <br> Professor Associado da Universidade de Coimbra |
| Member | Professor Doutor **António Manuel Gameiro Lopes** <br> Professor Auxiliar da Universidade de Coimbra |
| Advisor | Professor Doutor **Nuno Cláudio Ferreira Rosa** <br> Professor Auxiliar Convidado da Universidade de Coimbra |

**Coimbra, July, 2022**

Aguardo, equânime, o que não conheço —
Meu futuro e o de tudo.
No fim tudo será silêncio, salvo
Onde o mar banhar nada.

Ricardo Reis

Aos meus pais e irmão.

# ACKNOWLEDGEMENTS

First and foremost, I would like to express my gratitude to both my scientific advisors, Professor José Costa and Professor Nuno Rosa. Without their guidance and endless patience, this work would not have been possible.

I would also like to thank my friends who supported me, not only throughout this work but also during my entire graduation route. The memories of hard work in the library, pushing ourselves to become better, and the many laughs we shared will stay with me forever.

Finally, I wish to thank my family, especially my parents and brother, for their support, sacrifice and comprehension.

# Abstract

In the first attempts to return to normality after the initial impact of the COVID-19 pandemic, dentists were a class of professionals particularly vulnerable to contracting the disease. This is due to the fact that the production of respiratory particles and aerosols, resulting from the interaction between rotary tools and the patient's mouth, easily promotes the transmission of the virus. In order to respond to this problem, in 2020, STEsa, together with the Association for the Development of Industrial Aerodynamics (ADAI) and the Faculty of Medicine of the University of Coimbra (FMUC), developed a respiratory protection device (RPD) in the context of the MASK4MC (Mask for Medical Care) project. Through a specific design, this equipment combines the protective effects of a traditional visor and of an air curtain (aerodynamic sealing).

The main objectives of this work are the optimization of the prototype MASK4MC and the study of the influence of the user's respiration on the performance of its optimized configuration. The methodology followed to achieve these objectives was computational fluid dynamics (CFD), using the commercial software ANSYS CFX®. Three turbulence models − RNG $k$-$\varepsilon$, SST and BSL − were tested in order to assess the best adequacy to model the airflow field.

The optimization of the RPD was approached through the parametric study of the outlet velocities of the jets that form the air curtain and the tilt angle of one of them. Through this analysis, it was possible to conclude that the performance of the device generally increases as the velocity of the jets decreases and that the optimal value of the mentioned inclination angle depends on the velocity values considered.

Regarding the influence of the user's breathing on the device's performance, the results obtained show that respiration is relevant in the original design of the MASK4MC prototype and practically negligible in its optimized configuration.

The SST and BSL turbulence models led to very similar results in all the simulations performed, very often deviating from the predictions provided by the RNG model.

From the present work, it is concluded that the configuration considered optimal improves the protection efficiency of the original device by 24.1 % for the RNG model and by 33.8 % for the SST and BSL models.

# Resumo

Nas primeiras tentativas de regresso à normalidade depois do impacto inicial da pandemia COVID-19, verificou-se que os dentistas eram uma classe de profissionais particularmente vulnerável à contração da doença. A razão é a produção de partículas respiratórias, gotículas e aerossóis, resultantes principalmente da operação de ferramentas rotativas na boca do paciente, as quais facilmente transportam e transmitem o vírus. De modo a dar resposta a esta problemática, em 2020, a STEsa juntamente com a Associação para o Desenvolvimento da Aerodinâmica Industrial (ADAI) e a Faculdade de Medicina da Universidade de Coimbra (FMUC), desenvolveram um equipamento de proteção respiratória (EPR) no âmbito do projeto MASK4MC (Mask for Medical Care). Através de um desenho específico, este equipamento combina os efeitos de proteção de uma viseira tradicional (proteção mecânica) e de uma cortina de ar (vedação aerodinâmica).

Os objetivos principais deste trabalho consistem na otimização do protótipo MASK4MC e no estudo da influência da respiração do utilizador no desempenho do equipamento original e da configuração otimizada. A metodologia seguida para alcançar estes objetivos é a mecânica dos fluidos computacional (CFD, em inglês), utilizando o software comercial ANSYS CFX®. Foram testados três modelos de turbulência – RNG $k$-$\varepsilon$, SST e BSL – a fim de avaliar a melhor opção para modelar o campo de escoamento.

A otimização do EPR foi abordada através do estudo paramétrico das velocidades dos jatos que formam a cortina de ar e do ângulo de inclinação de um deles. Através desta análise foi possível concluir que a performance do dispositivo aumenta, geralmente, à medida que a velocidade dos jatos diminui e que a inclinação ótima do ângulo mencionado depende dos próprios valores de velocidade considerados.

Relativamente à influência da respiração do utilizador no desempenho do dispositivo, os resultados obtidos demonstram que esta é relevante na configuração original e praticamente desprezável na configuração otimizada.

Os modelos de turbulência SST e BSL tiveram resultados muito semelhantes em todas as simulações realizadas, afastando-se, com muita frequência, das previsões fornecidas pelo modelo RNG.

Neste trabalho, a configuração considerada ótima, melhora a proteção do dispositivo original em 24.1 % para o modelo RNG e em 33.8 % para os modelos SST e BSL.

**Palavras-chave:**    EPR, MASK4MC, Cortina de ar, Estudo paramétrico, Influência respiratória, CFD.

# Contents

# LIST OF FIGURES

# LIST OF TABLES

# LIST OF SIMBOLS AND ACRONYMS

## Symbols

$C_{\varepsilon 1RNG}$ – Function present in the RNG turbulence model

$C_{\varepsilon 2RNG}$ – Constant of the RNG turbulence model

$C_{ij}$ – Transport of $R_{ij}$ by convection

$C_{\mu}$ – Constant of the RNG turbulence model

$D_{ij}$ – Transport of $R_{ij}$ by diffusion

$k$ – Turbulent kinetic energy

$P$ – Pressure

$P_{ij}$ – Rate of production of $R_{ij}$

$P_k$ – Turbulence production due to viscous forces in the RNG turbulence model

$R_{ij}$ – Kinematic Reynolds stresses

$t$ – Time

$\mathbf{u}$ – Fluid's velocity vector

$\mathbf{u}'$ – Velocity fluctuations vector

$u_{\tau}$ – Friction velocity

$V_1, V_2, V_3, V_4$ – Velocity module of jets one, two, three and four

$y^+$ – Dimensionless distance from the wall

## Greek Symbols

$\delta_{ij}$ – Krönecker delta

$\Delta y$ – Distance to the wall of the first node of the mesh

$\varepsilon$ – Rate of dissipation of turbulent kinetic energy

$\varepsilon_{ij}$ – Rate of dissipation of $R_{ij}$

$\theta_4$ – Tilt angle of the fourth jet

$\mu$ – Dynamic viscosity of the fluid

$\mu_t$ – Turbulent viscosity of the flow

$\nu$ – Kinematic viscosity of the fluid

$\Pi_{ij}$ – Transport of $R_{ij}$ due to turbulent pressure-strain interactions

$\rho$ – Fluid's density

$\sigma_k$, $\sigma_{\varepsilon RNG}$ – Constants of the RNG turbulence model

$\tau_{ij}$ – Reynolds stresses

$\tau_\omega$ – Wall shear stress

$\omega$ – Turbulence frequency

$\Omega_{ij}$ –Transport of $R_{ij}$ due to rotation

## Acronyms

ADAI – Association for the Development of Industrial Aerodynamics

CFD – Computational Fluid Dynamics

CAD – Computer Aided Design

FMUC – Faculty of Medicine of the University of Coimbra

MASK4MC – Mask for Medical Care

PF – Protection Factor

RANS – Reynolds-Averaged Navier-Stokes

RPD – Respiratory Protection Device

# 1. INTRODUCTION

In this chapter the motivation that led to this work is presented as well as a revision of the work already developed by the project MASK4MC and a compilation of the improvements required. The objectives of the thesis and a description of each chapter are also laid out.

## 1.1. Context

The COVID-19 pandemic created a global and growing concern with the protection against viruses that are transmitted by respiratory droplets (particle size greater than 5 micron) or aerosols (particle size below 5 micron). Also, very early in the pandemic it was understood that the key to control the spread of the virus would be the use of respiratory protection devices (RPD), such as facial masks or visors, and appropriate ventilation.

One group of people that is evidently exposed to the transmission of this sort of biological contaminants are dentists. While they work, dentists are in contact with respiratory-born droplets and with aerosols produced by the interaction of the rotary equipment with their patient's mouth. In order to prevent contamination, the use of RPD is mandatory as well as good ventilation of the working space. The project MASK4MC considered these two aspects.

MASK4MC was a time-intensive research project started in the early period of the COVID-19 pandemics, aimed at developing an individual protective device for medical professionals based on a visor provided with aerodynamic sealing of the breathing zone. After several intermediate versions, it came up with a prototype whose characteristics proved the protection effectiveness of the original concept, while guaranteeing the set of strict specifications required by dentists' activities. The components of this RPD (Figure 1.1) are a face shield, that offers the same physical protection as a normal visor, a plenum that produces an air curtain, an inlet air pipe that provides the required air, and a support system that allows the fixing of the equipment to the user's head. The use of an air curtain enables the sealing of the user's breathing zone by limiting the mass transfer between the protected

area, which is cleaned, and the external environment, which is polluted (Moureh & Yataghene, 2016).

Computational Fluid Dynamics (CFD) was used in the model construction and the study of the prototype MASK4MC. This approach allowed a prompt study of numerous configurations of the RPD. In this work, the same methodology is used to study and optimize the configuration of the latest prototype developed.
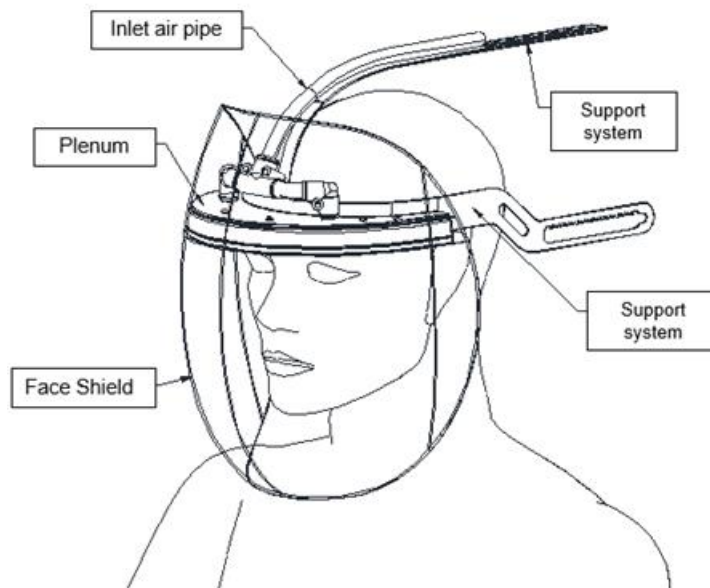


**Figure 1.1.** Components of the prototype MASK4MC.

## 1.2. The MASK4MC prototype

The latest MASK4MC prototype developed was provided with the plenum shown in Figure 1.2. This plenum used two perforated filters that promoted a pressure drop in the airflow and allowed a reasonable control of the air velocity intensity and the direction of the jets 1, 2 and 3, that can be seen in Figure 1.3. The airflow feeding the fourth jet followed a free path, i.e., without any filters' pressure drop. The airflow streamlines inside the plenum and the outlet velocity vector of the four jets are illustrated in Figure 1.4 and Figure 1.5, respectively. A cascade effect was promoted on the plenum, due to its geometry, that in combination with the filters' pressure drop results in a relatively uniform velocity of the jets,

which was intended. As expected, the velocity distribution of the fourth jet was less uniform than the other jets.



(a)                                          (b)
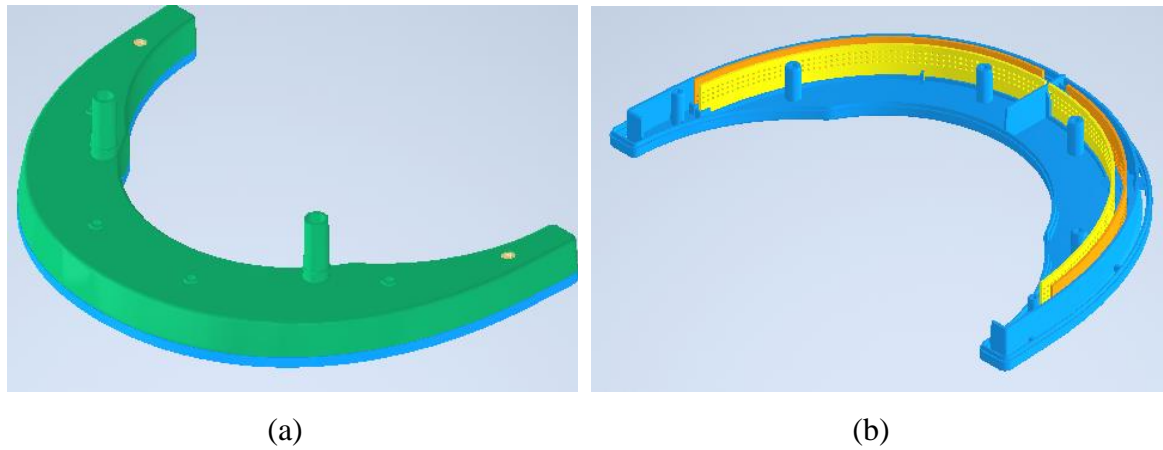
**Figure 1.2.** Plenum's geometry of the latest MASKS4MC prototype: (a) with the cover; (b) without cover.
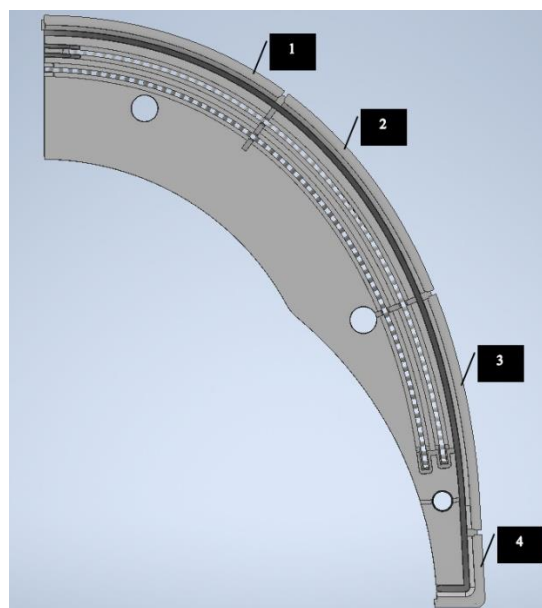


**Figure 1.3.** Plenum's air domain of the MASK4MC prototype model. The jet outlets are indicated.
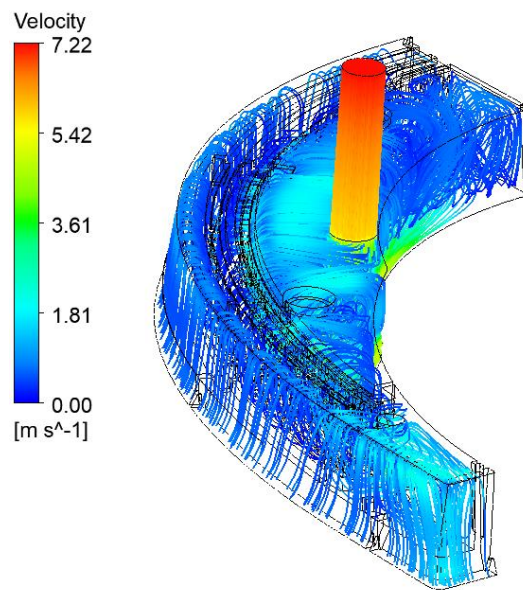
**Figure 1.4.** Airflow streamlines inside the plenum of the latest MASK4MC prototype.
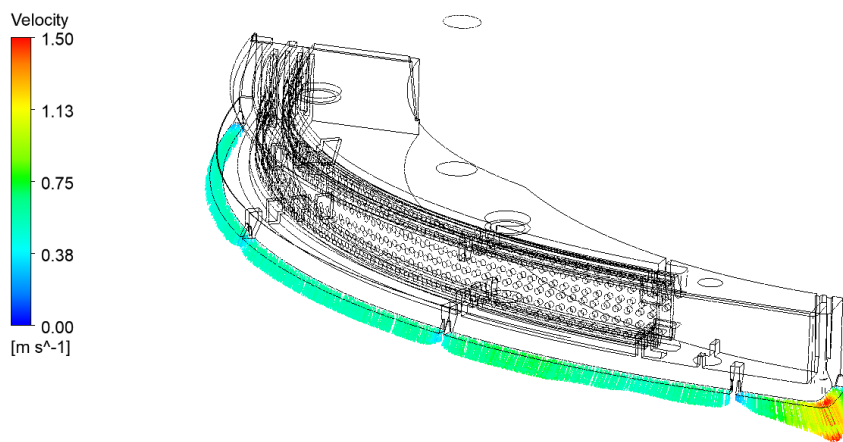


**Figure 1.5.** Outlet velocity vectors of the four jets of latest MASK4MC prototype.

The air curtain that resulted from the plenum mentioned is illustrated in Figure 1.6. One can see that the flow separated from the visor shield and that the airflow from the fourth jet was somehow entrained into the breathing zone. Nevertheless, the air curtain was quite uniform and stable. The protection effect, assessed as a sealing efficiency, provided by the device was approximately 68.3 %, based on the numerical results with the RNG turbulence model and the second mesh mentioned in the second chapter of this work. The protection

efficiency drops down to 45.5 %, when estimated after the simulation results obtained with the SST and BSL turbulence models.



(a)                                      (b)
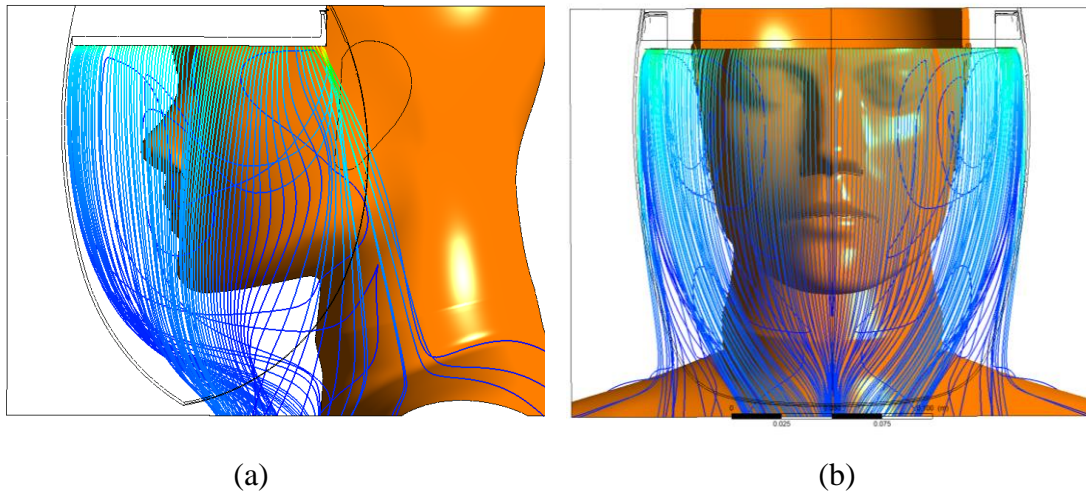
**Figure 1.6.** Air curtain (CFD) of the latest MASK4MC prototype: (a) side view; (b) front view.

Finally, this prototype was pared with side flaps (Figure 1.7) in order to reduce the side effects mentioned earlier. The efficiency estimated, in this case, was approximately 100 % (Consórcio MASK4MC Instituição, 2021). This last model, however, would require more material to be produced and a custom-made policy.
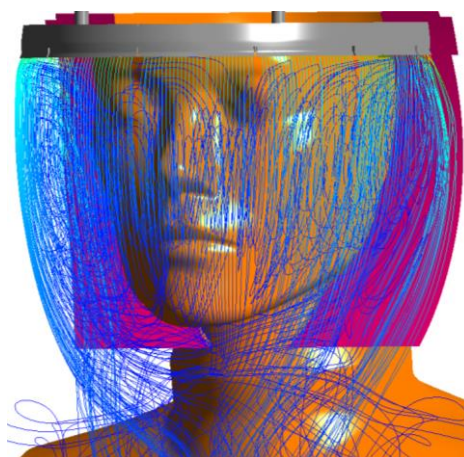


**Figure 1.7.** Air curtain (CFD) of the latest MASK4MC prototype with side flaps.

## 1.3.   Necessary optimizations

Taking into consideration what has been exposed so far, one concludes that there was a need to optimize the prototype presented. Optimizations of the air curtain and of the plenum that produces it were necessary. This text, however, addresses only the problems regarding the air curtain. The main problems to improve were the following ones: the entrainment of the fourth jet and the sealing efficiency.

The prior studies of the RPD also lacked in two aspects. The first one is that the effect of breathing has not been considered. Wei et al. (2021) showed that the respiration phenomenon greatly reduces the sealing efficiency of the air curtain. Obviously, the use of face masks reduces the risks of this effect. However, in order to increase the range of application of the RPD, the scrutiny of such aspect is relevant. The use of only one turbulence model is the other weak point of previous studies. Because of the flow separation and the formation of vortices, the flow inside the visor was quite complex and the modeling of turbulence was not a straightforward process. Therefore, an analysis of it with different turbulence models would provide more data to compare with experimental information. This, in turn, would validate the numerical model.

## 1.4.   Objectives and structure of the work

The objectives of this work were: (1) to optimize the MASK4MC prototype, modeling the user's breathing and (2) to study its effect on the performance of both the RPD prototype and its optimized configuration; and (3) to use two other turbulence models and compare the results obtained.

This thesis is divided into four chapters. The first one serves as an introduction to the reader to both the MASK4MC project and the work developed in this thesis. In the second chapter the numerical modeling of the problem is presented. In the third chapter the results obtained for each case studied are exposed and analyzed. Finally, in the last chapter, the main conclusions withdrawn from the work are addressed.

# 2. NUMERICAL MODELING

In this chapter it will be analyzed the numerical model used to study the RPD performance. First, the geometry of the model is shown, followed by the numerical method. Then, the cases studied are exposed as well as the tests for mesh independency. After that, the boundary and initial conditions of the model are specified. The chapter ends with the definition of the so-called "Protective Factor" (PF).

## 2.1. Simulated geometry

The geometry of the numerical model consisted of three components: the RPD, without the air distribution system, a thermal mannequin and an exterior volume of air with dimensions $287 \times 130 \times 279$ mm that encapsulates the prior components mentioned. This geometry is shown in Figure 2.1.
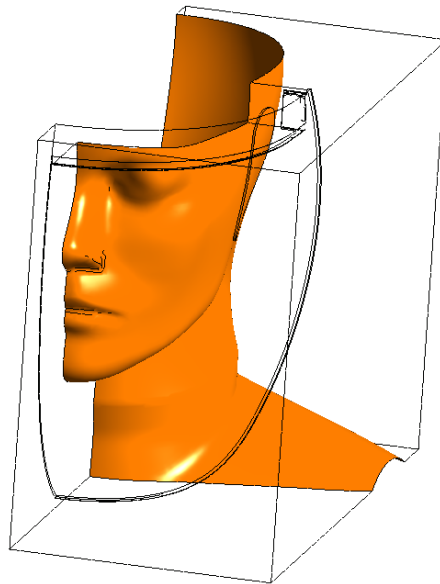


**Figure 2.1.** Geometry of the calculation domain.

## 2.2. Numerical method and solution procedure

The commercial code ANSYS CFX® was utilized to study the behavior of the RPD. Three turbulence models were comparatively used: the SST model, the RNG model and the BSL Reynolds stress model.

Two different types of studies were conducted. One, without considering the respiration process of the mannequin, and the other with this process implemented in the model. For both of them, it was assumed air at 25℃. The first one was assumed to be a steady state process, and the second a transient process.

Convergence was assumed to be achieved when all residuals became lower than $10^{-6}$ or when the concentration of polluted air in the monitoring points inside the RPD was constant.

### 2.2.1. Turbulence models

The previously mentioned turbulence models have the same origin, the Reynolds-Averaged Navier-Stokes equations (RANS):

$$\frac{\partial u}{\partial t} + div(u\mathbf{u}) = -\frac{1}{\rho}\frac{\partial P}{\partial x} + v\,div(grad(u)) - div(\overline{u'\mathbf{u}'}), \tag{2.1}$$

$$\frac{\partial v}{\partial t} + div(v\mathbf{u}) = -\frac{1}{\rho}\frac{\partial P}{\partial y} + v\,div(grad(v)) - div(\overline{v'\mathbf{u}'}), \tag{2.2}$$

$$\frac{\partial w}{\partial t} + div(w\mathbf{u}) = -\frac{1}{\rho}\frac{\partial P}{\partial z} + v\,div(grad(w)) - div(\overline{w'\mathbf{u}'}), \tag{2.3}$$

where $u$, $v$ and $w$ are the components of the fluid's velocity vector, $\mathbf{u}$, regarding the $x$, $y$ and $z$ axis at time $t$, $P$ is pressure, and $\rho$ and $v$ are the fluid's density and kinematic viscosity, respectively. It is important to note that the operator $\bar{h}$, applied to a generical variable, $h$, corresponds to the time average of that variable. In Eqs. (2.1), (2.2) and (2.3) one can also find the velocity fluctuations vector $\mathbf{u}'$, with components $u'$, $v'$ and $w'$ that characterize the turbulent flow, and that create the so-called Reynolds stresses:

$$\tau_{ij} = -\rho\overline{u'_i u'_j}, \text{ with } i,j = 1,2,3. \tag{2.4}$$

These Reynolds stresses actually represent the effect of turbulence, i.e., an extra mechanism of momentum transport in the fluid, and their value is frequently far greater than their viscous

counterpart. The challenge of turbulence modeling is to accurately take into consideration these additional six terms.

### 2.2.1.1. RNG $k$-$\varepsilon$ model

This turbulence model takes into consideration the Reynolds stresses through the Boussinesq hypothesis:

$$\tau_{ij} = -\rho\overline{u'_i u'_j} = \mu_t\left(\frac{\partial u_i}{\partial x_j} + \frac{\partial u_j}{\partial x_i}\right) - \frac{2}{3}\rho k\delta_{ij}, \text{ com } i,j = 1,2,3, \tag{2.5}$$

where $\mu_t$ is the so-called turbulent viscosity of the flow, $k$ is the turbulent kinetic energy of the flow and $\delta_{ij}$ is the Krönecker delta ($\delta_{ij} = 1$, if $i = j$, and $\delta_{ij} = 0$, if $i \neq j$). The turbulent kinetic energy is, by definition, given by:

$$k = \frac{1}{2}\left(\overline{u'^2} + \overline{v'^2} + \overline{w'^2}\right), \tag{2.6}$$

and is related to $\mu_t$, in this turbulence model, by:

$$\mu_t = \rho C_\mu\frac{k^2}{\varepsilon}, \tag{2.7}$$

where $\varepsilon$ is the rate of dissipation of turbulent kinetic energy per unit mass and $C_\mu$ is a constant (Ansys CFX-Solver Modeling Guide, 2022).

Therefore, regarding this turbulence model, the problem focuses on the calculation of $k$ and $\varepsilon$. This is solved using two additional transport equations ("two-equation turbulence model"), one for each new variable:

$$\frac{\partial(\rho k)}{\partial t} + \frac{\partial(\rho u_j k)}{\partial x_j} = \frac{\partial}{\partial x_j}\left[\left(\mu + \frac{\mu_t}{\sigma_k}\right)\frac{\partial k}{\partial x_j}\right] + P_k - \rho\varepsilon, \tag{2.8}$$

and

$$\frac{\partial(\rho\varepsilon)}{\partial t} + \frac{\partial(\rho u_j\varepsilon)}{\partial x_j} = \frac{\partial}{\partial x_j}\left[\left(\mu + \frac{\mu_t}{\sigma_{\varepsilon RNG}}\right)\frac{\partial\varepsilon}{\partial x_j}\right] + \frac{\varepsilon}{k}(C_{\varepsilon 1RNG}P_k - C_{\varepsilon 2RNG}\rho\varepsilon), \tag{2.9}$$

where $\sigma_k$, $\sigma_{\varepsilon RNG}$, $C_{\varepsilon 2RNG}$ are constants, $\mu$ is the dynamic viscosity of the fluid, $P_k$ is the rate of turbulence production of $k$ due to viscous forces, calculated via:

$$P_k = \mu_t\left(\frac{\partial u_i}{\partial x_j} + \frac{\partial u_j}{\partial x_i}\right)\frac{\partial u_i}{\partial x_j}, \tag{2.10}$$

and $C_{\varepsilon 1RNG}$ is a function of $k$, $\varepsilon$ and the rate of strain of the fluid (Ansys CFX-Solver Theory Guide, 2022).

This turbulence model is numerically stable and robust according to Ansys CFX-Solver Modeling Guide (2022), but does not accurately predict flows with boundary layer

separation and rotating fluids (complex flows). It also fails in modeling the flow in the near-wall region, where $\varepsilon \to 0$.

### 2.2.1.2. SST model

This is a hybrid model that uses the standard $k\text{-}\varepsilon$ model in the fully turbulent region of the flow and in the near-wall region transforms it into a $k\text{-}\omega$ model, which uses the turbulence frequency

$$\omega = \frac{\varepsilon}{k}. \tag{2.11}$$

This turbulence model is suitable for boundary layer flows and allows a more refined wall treatment when compared with the RNG model.

### 2.2.1.3. BSL model

This turbulence model does not use the turbulence or eddy viscosity as the previous two do; instead, it directly computes the Reynolds stresses. In this model, there are seven more transport equations to solve, six related to the Reynolds stresses and one related to $\omega$. Versteeg & Malalasekera (2007) defines the Reynolds stresses transport equations in the following way:

$$\frac{\partial R_{ij}}{\partial t} + C_{ij} = P_{ij} + D_{ij} - \varepsilon_{ij} + \Pi_{ij} + \Omega_{ij}, \text{ com } i, j = 1,2,3, \tag{2.12}$$

where

$$R_{ij} = -\frac{\tau_{ij}}{\rho} = \overline{u'_i u'_j}, \text{ com } i, j = 1,2,3, \tag{2.13}$$

and $C_{ij}$ corresponds to the transport of $R_{ij}$ by convection, $P_{ij}$ is the rate of production of $R_{ij}$, $D_{ij}$ is the transport of $R_{ij}$ by diffusion, $\varepsilon_{ij}$ is the rate of dissipation of $R_{ij}$, $\Pi_{ij}$ is the transport of $R_{ij}$ due to turbulent pressure-strain interactions and $\Omega_{ij}$ represents the transport of $R_{ij}$ due to rotation.

This turbulence model is suitable for free shear flows with strong anisotropy and with strong streamline curvature. Meanwhile, because this model solves seven, instead of just two additional transport equations, the computing cost of this one is much greater than the other two models.

## 2.2.2. Wall treatment

It is well known that the boundary layer in the near-wall region of the flow can be divided in three layers (L. A. Oliveira & A. G. Lopes, 2016): the laminar or viscous sublayer, the buffer layer and the logarithmic layer. This division is based on the relative magnitude of the viscous and Reynolds stresses. In the laminar sublayer, the viscous stresses are greater than the Reynolds stresses, while in the logarithmic layer the opposite is observed. In the buffer layer the magnitude of both is similar. This last layer will not be considered in the following analysis, i.e., the so-called concept of two-layer near-wall flow region. The size of the viscous layer will depend on the flow Reynolds number. Higher Reynolds numbers create smaller viscous layers. Therefore, depending on the Reynolds number, one can either neglect the laminar sublayer or not.

The software Ansys CFX® has two types of wall treatment: a scalable function treatment or an automatic treatment. The first one avoids solving the flow domain throughout the viscous layer, while the latter does not. Depending on the turbulence model, the treatment available will vary.

### 2.2.2.1. Scalable function treatment

The scalable function approach was utilized with the RNG model. This treatment uses a logarithmic wall-function that bridges the calculation from the near-wall first node up to the wall, thus avoiding the need for a very refined grid as it would be the case to adequately solve the viscous sublayer.

By default, the scalable function considers a value of $y^+$, the dimensionless distance from the wall, equal to $11.06$ for the transition of the two layers previously mentioned (with no buffer layer), with $y^+$ given by:

$$y^+ = \frac{\rho \, \Delta y \, u_\tau}{\mu}, \qquad (2.14)$$

where $\Delta y$ is the distance to the wall of the first mesh node (Ansys CFX-Solver Theory Guide, 2022), and $u_\tau$ is the friction velocity defined as:

$$u_\tau = \left(\frac{\tau_\omega}{\rho}\right)^{1/2}, \qquad (2.15)$$

with $\tau_\omega$ as the wall shear stress. Therefore, all wall-adjacent nodes in the flow domain can be located outside the viscous sublayer, i.e, at $y^+ > 11.06$, thus allowing significant savings in the computational resources and time required.

#### 2.2.2.2. Automatic treatment

The automatic approach was utilized with the SST and BSL models. Depending on how refined the mesh is, this treatment either uses the logarithmic wall function, for coarser grids, or solves the transport equations all the way to the wall, for refined grids. The switch between these two methods is also based on the value of $y^+$, like previously explained. A maximum value of $y^+$ lower than 11.06 now means that the wall function will not be utilized. This enables a more accurate study of the boundary layer because the viscous layer is now solved up to the wall surface.

### 2.2.3. Multiphase flow model

In order to determine the PF of the RPD, a multiphase flow model was utilized. This model considers two fluids: contaminated air and cleaned air. The first one simulates the polluted air of the environment and the second one the air provided by the RPD. Both fluids have the same physical properties, since they were both at 25 ℃ and at atmospheric pressure. The interaction of these two fluids is simulated with a mixture model with the following characteristics: an interface length scale equal to 0.00033 micron and a value of 0.44 for the drag coefficient. A single turbulence field was determined for both fluids (homogenous turbulence option).

## 2.3. Cases

Three studies were carried out. Firstly, an optimization of the original prototype of the RPD was conducted without the simulation of the user's breathing. Then, the effect of breathing on the original prototype was studied. Finally, the influence of the breathing process in the optimized version was also studied.

### 2.3.1. Optimization of the prototype

In this case study, the jet velocities and the tilt angle of the fourth jet were analyzed in order to maximize the PF and minimize the drawbacks of the RPD already mentioned. Firstly, different sets of jet velocity values, presented in Table 2.1, were studied. $V_1$, $V_2$, $V_3$ and $V_4$ correspond to the module of the outlet velocity of jets 1, 2, 3, and 4, respectively. $V_4$ was computed so that the momentum of the fourth jet was equal to the sum of the momentum

of the other three jets, in order to solve, or at least decrease, the entrainment of the air issued by this jet into the breathing zone. These simulations also allowed the study of the effect on the PF of varying the jets' velocity.

Then, for the set of jet velocities considered, the tilt angle of the fourth jet, $\theta_4$, was varied between the values of 0° and 80°, with an increment of 20°. The model specifications providing the higher PF across the three turbulence models was utilized in the simulation with the breathing process mentioned above.

**Table 2.1.** Sets of jet velocity values considered for the optimization study.

| **Velocity set** | $V_1$ [m/s] | $V_2$ [m/s] | $V_3$ [m/s] | $V_4$ [m/s] |
|:---:|:---:|:---:|:---:|:---:|
| 1 | 0.5 | 0.5 | 0.5 | 1.74 |
| 2 | 0.4 | 0.4 | 0.4 | 1.39 |
| 3 | 0.3 | 0.3 | 0.3 | 1.04 |
| 4 | 0.2 | 0.2 | 0.2 | 0.7 |
| 5 | 0.1 | 0.1 | 0.1 | 0.35 |
| 6 | 0.6 | 0.6 | 0.4 | 1.91 |

## 2.3.2. Simulation of the breathing process

In the last two studies, the user's respiration was considered. This process is transient and was modulated as such. Based on the work developed by Gao & Niu (2006), one can simulate the air flow of respiration as a harmonic function, like the one presented in Figure 2.2 (only three cycles were studied).
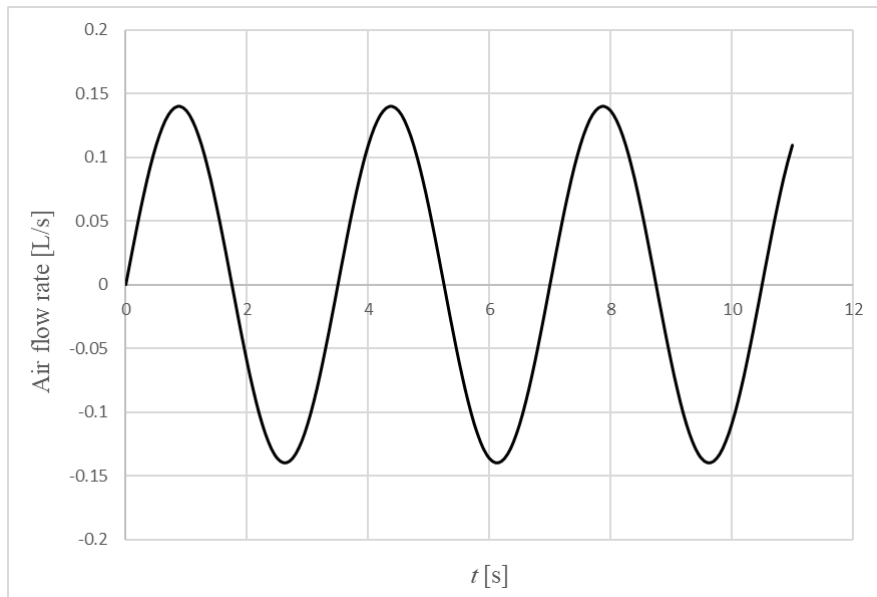
**Figure 2.2.** Evolution of the air flow rate during the respiration process.

In this case, the airflow rate, $\dot{Q}$, is given, in liters per second, by:

$$\dot{Q} = 0.14 \sin(1.8t). \tag{2.16}$$

The air velocity, in meters per second, was considered uniform in the area of the nostrils, $A_{nostrils}$, consequently its module can be calculated in the following way:

$$V = \frac{0.14 \sin(1.8t)}{A_{nostrils}} \times 10^{-3}. \tag{2.17}$$

Only respiration through the nose was considered. $A_{nostrils}$ was taken from the Computer Aided Design (CAD) model of the thermal mannequin and the value obtained was:

$$A_{nostrils} = 148.738 \times 10^{-6} \; m^2. \tag{2.18}$$

## 2.4. Tests for mesh and time step independence

Using the original model of the RPD, tests for mesh and time step independence were carried out. Three meshes were used with two inflation layers, equally defined, one in the vicinity of the visor and another next to the face of the thermal mannequin. Each layer had 15 levels with a growth rate between levels of 1.2. The distance to the wall of the first node of the layer was different in each mesh. The element size in the remaining domain also varied. Details of the three meshes can be found in Table 2.2.

**Table 2.2.** Characteristics of the meshes utilized.

|  | 1st Mesh | 2nd Mesh | 3rd Mesh |
|---|---|---|---|
| **Element size [m]** | 0.005 | 0.0025 | 0.0015 |
| **Distance to the wall of the 1st node [m]** | 0.001 | 0.0001 | 0.0001 |
| **Nº of nodes** | 86799 | 694794 | 2841293 |

Since respiration is a transient process, a test for time step independence was also performed. The time steps tested were: $0.5$ s, $0.1$ s and $0.05$ s.

### 2.4.1. Mesh independence

In order to verify the mesh independence, the velocity and the contaminant fraction of a set of points was determined. The points selected to measure the velocity are shown in Figure 2.3, while the ones chosen to measure the contaminant fraction are represented in Figure 2.4. The values obtained for each mesh were then compared. This process was carried out for the three turbulence models. The mesh adopted for the remaining study was the second one since it was the mesh with the higher ratio of precision-to-computational cost.



(a)                                        (b)
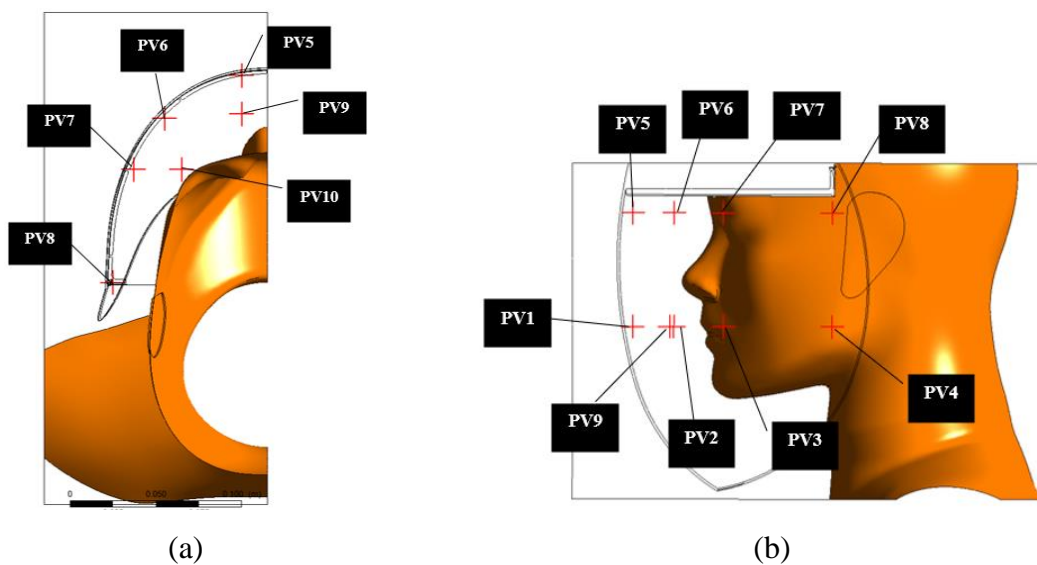
**Figure 2.3.** Points used to measure the velocity for the mesh independence test: (a) top view; (b) side view.

(a)                                                              (b)
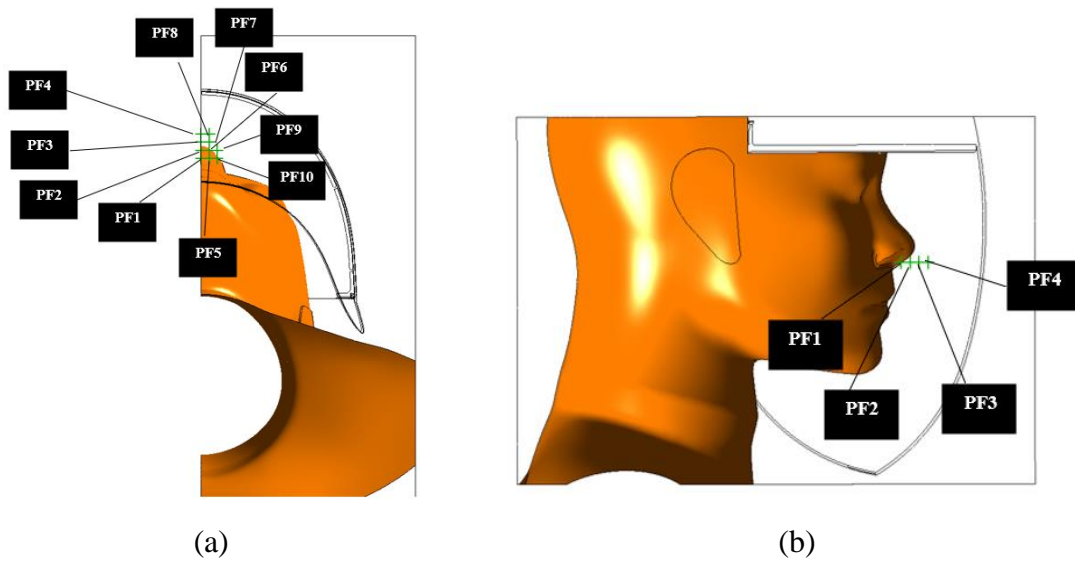
**Figure 2.4.** Points used to measure the contaminant fraction for the mesh independence test: (a) top view; (b) side view.

### 2.4.1.1.   RNG *k-ε* model

The velocity distribution for this model is presented in Figure 2.5. One can see that there is a great resemblance between the results obtained with the three different meshes and also that the variation of velocity is very similar for all meshes.

The contaminant fraction distribution for this model is presented in Figure 2.6. This time, the similarity is quite small, but the values get closer as the mesh gets refined.

Based on this analysis, it is safe to conclude that this turbulence model displayed numerical convergence regarding the grid dependence.
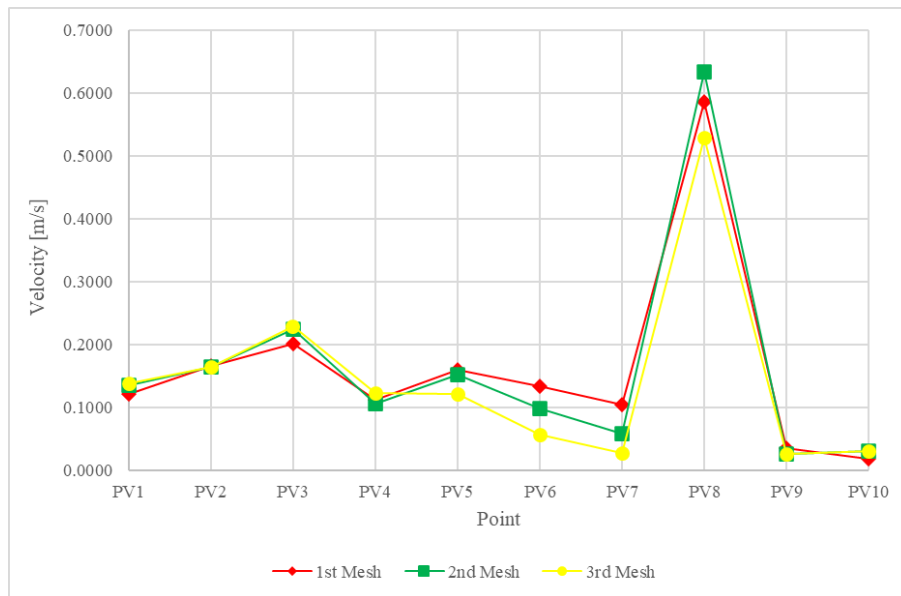
**Figure 2.5.** Mesh independence test (velocity) of the RNG $k$-$\varepsilon$ model.
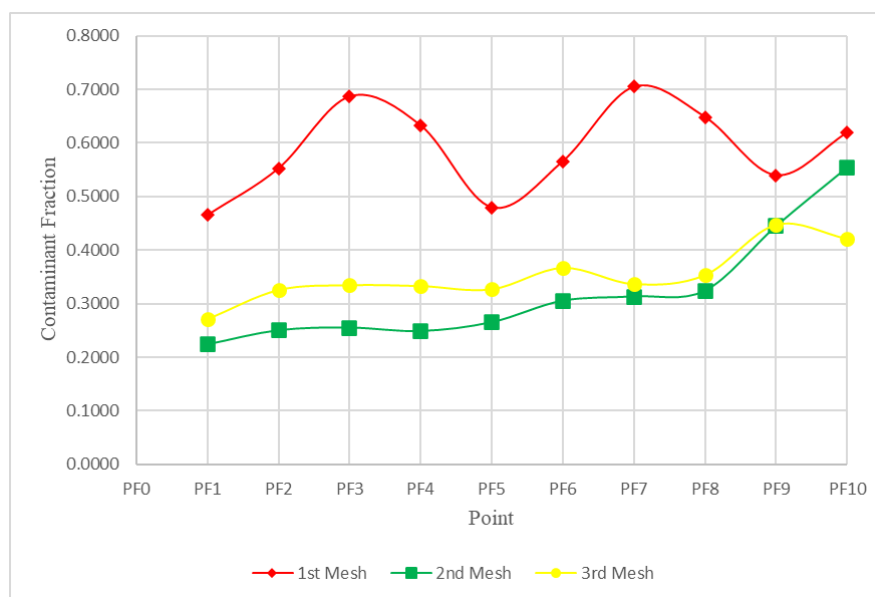


**Figure 2.6.** Mesh independence test (contaminant fraction) of the RNG $k$-$\varepsilon$ model.

### 2.4.1.2. SST and BSL models

The velocity distribution computed for both models is quite similar and is presented in Figure 2.7, for the SST model, and in Figure 2.8, for the BSL model. Once again, there is some overlap between the values of the three different meshes, but not quite as much as the one found in the first turbulence model. The variation of velocity is identical in all cases.
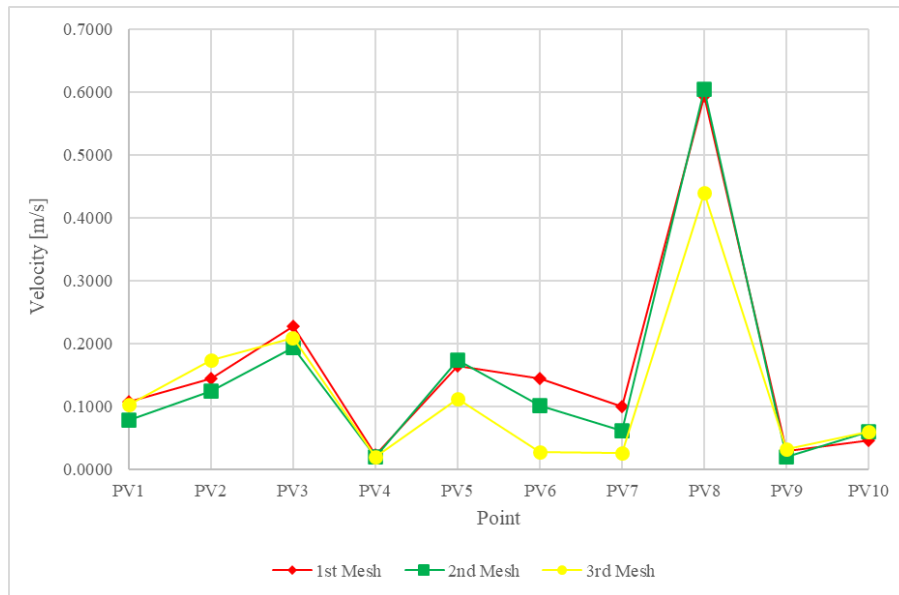
**Figure 2.7.** Mesh independence test (velocity) of the SST model.
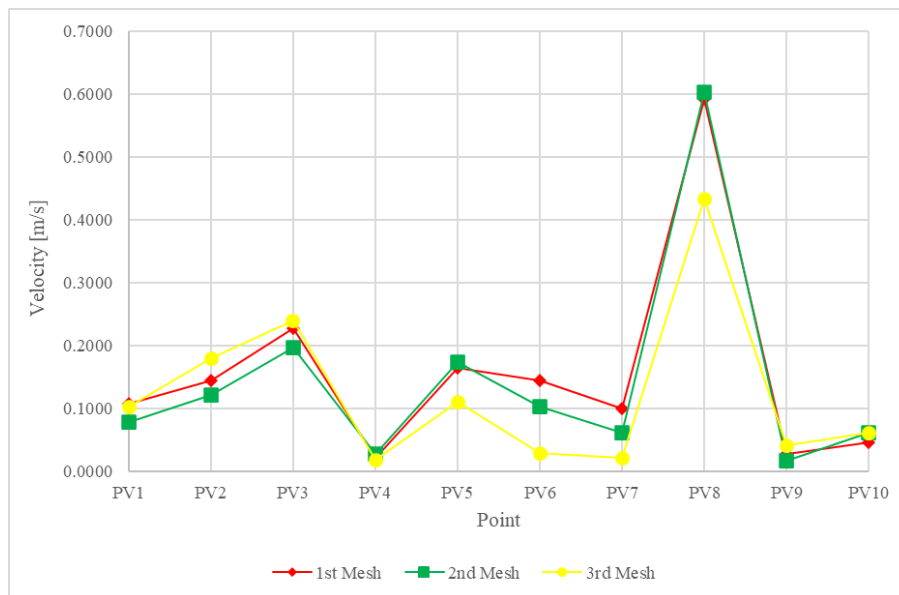


**Figure 2.8.** Mesh independence test (velocity) of the BSL model.

Figure 2.9 and Figure 2.10 represent the contaminant fraction distributions for the SST and BSL models, respectively. The behavior of the values is quite similar to the one found for the RNG model, but this time, as the mesh gets refined the contaminant fraction gets larger.
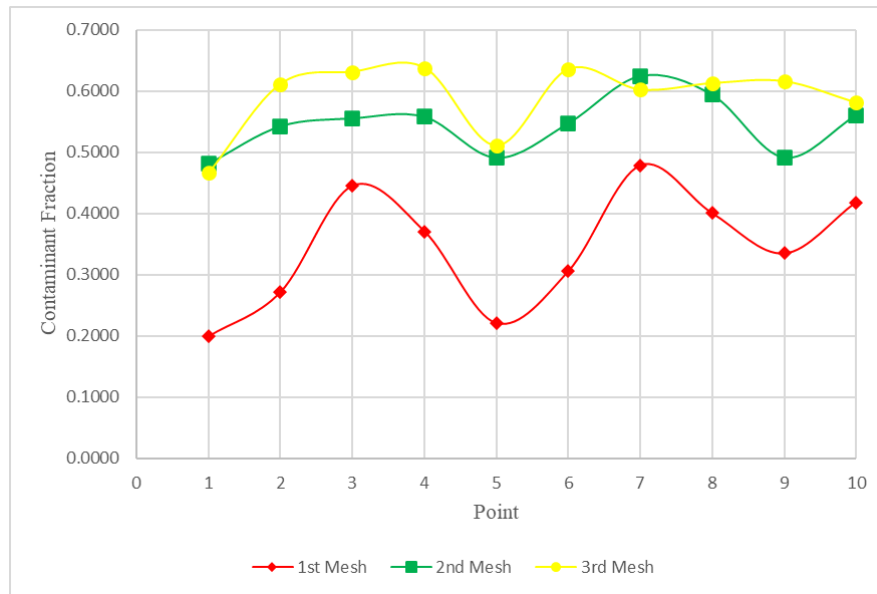
**Figure 2.9.** Mesh independence test (contaminant fraction) of the SST model.
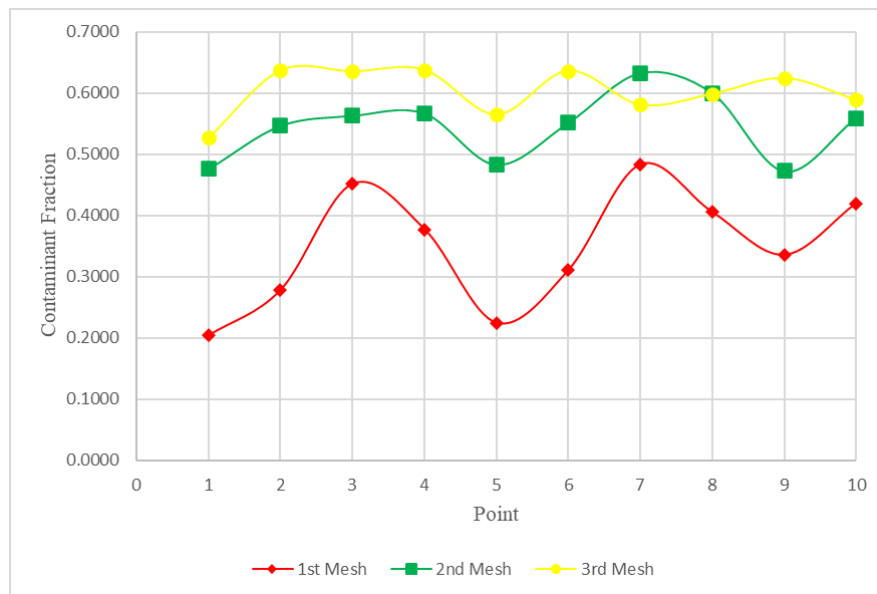


**Figure 2.10.** Mesh independence test (contaminant fraction) of the BSL model.

Once again, numerical convergence was achieved for both models.

## 2.4.2. Time step independence

In order to verify the time step independence, the time evolution of the velocity of PV9 and of the contaminant fraction of PF1 were determined; they are presented in Figure 2.11

and Figure 2.12, respectively. This procedure was carried out only for one turbulence model, the RNG model. It was assumed that the behavior of the other turbulence models would be similar, which is reasonable since the time rate of change of both the velocity and contaminant fraction is expected to be analogous for each of them. Analyzing both figures, one can see, firstly, that the variation of velocity and contaminant fraction is very similar for every time step considered. Additionally, it is also clear that there is a great similarity between the results obtained with each time step, especially for the last two. Taking this into consideration, the time step adopted for further analysis was the second one, since it had the highest precision-to-computational ratio.
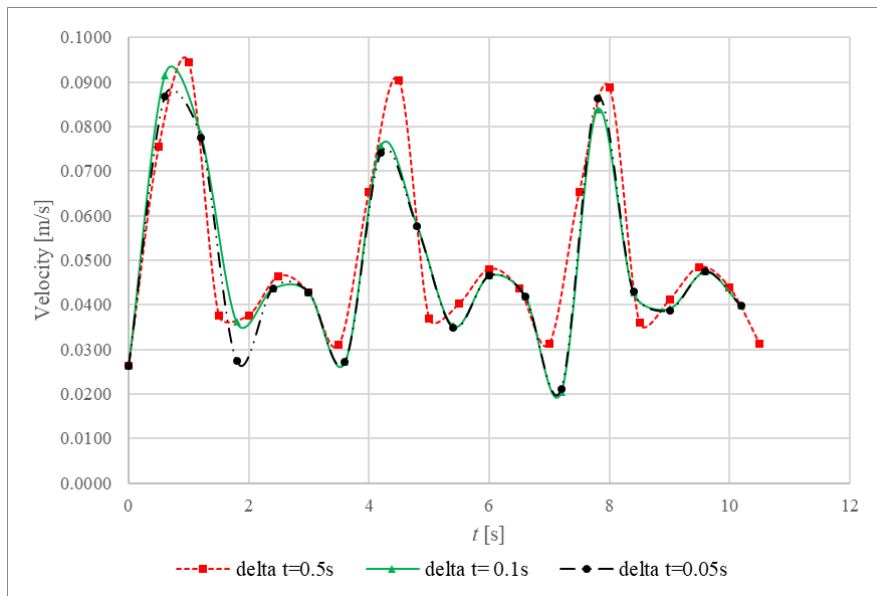


**Figure 2.11.** Time step independence test (velocity) of the RNG model.
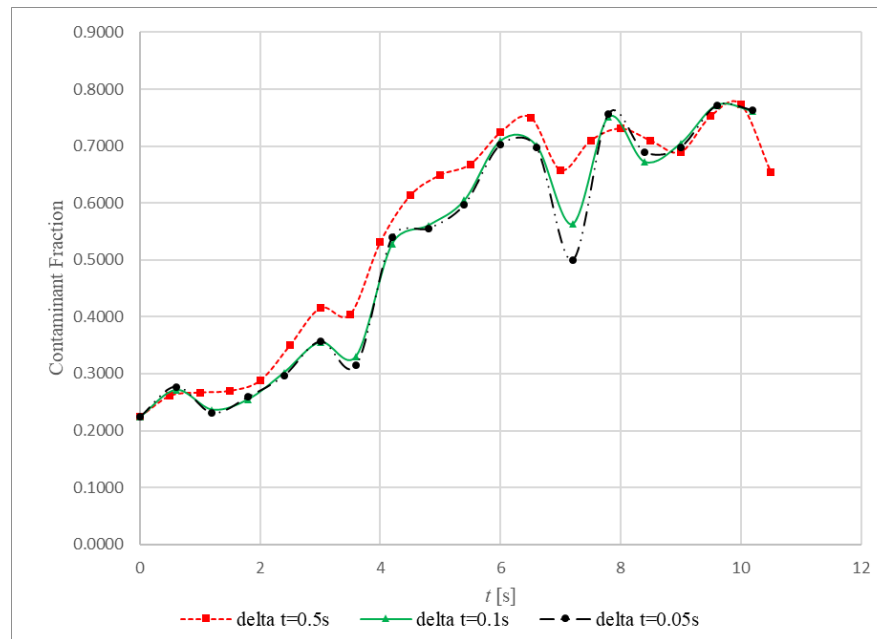
**Figure 2.12.** Time independence test (contaminant fraction) of the RNG model.

## 2.5. Boundary and initial conditions

Four boundary conditions were defined. The exterior boundaries of the domain were defined as an opening where only contaminant air enters with a turbulence intensity equal to 5%. The jet inlets were defined as inlets of cleaned air with a defined velocity normal to the entrance surfaces. The turbulence intensity was assigned a value of 5%. The mannequin head and the visor surface were defined as walls with no slip. Since only half of the geometry was simulated, a symmetry condition also had to be defined. The representation of this boundary conditions in ANSYS CFX® can be found in Figure 2.13. For the respiration case, one more boundary condition had to be defined. The surface of the mannequin corresponding to the outlet of the nostril was defined as an inlet of cleaned air with a velocity profile equal to the one already mentioned for the respiration process. The turbulence intensity for this inlet was also 5%.
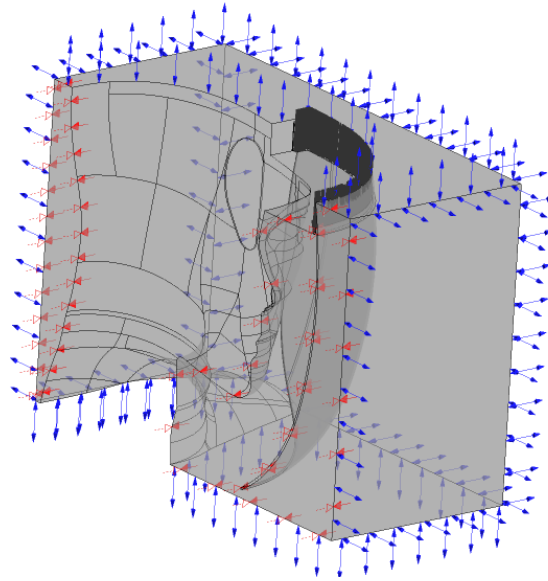
**Figure 2.13.** Representation of the boundary conditions of the model with no respiration in ANSYS CFX®.

The initial conditions depended on whether respiration was taken into consideration or not. If not, then the initial velocity field was zero. Otherwise, the converged results of the simulation with no respiration were used as the initial conditions for the analogous simulation with respiration.

## 2.6. Protective factor

In order to determine the protection of the RPD, a PF was determined. The calculation of this PF depended on whether respiration was considered or not.

In the case of no respiration, in order to compute the PF, the average contaminant fraction was first calculated, based on the values of contaminant fraction measured in the set of points mentioned before. The PF was then defined in the following way:

$$PF = (1 - average\ contaminant\ fraction) \times 100, \tag{2.19}$$

With respiration, the process was quite similar. Initially, the average contaminant fraction was also determined the same way, but this time this calculation was carried out in the beginning of the simulation, the finale, and every 0.6 seconds in between. After that, the time average of the different spatial averages was determined. The PF was then defined in the following way:

$$PF = (1 - time\ average\ contaminant\ fraction) \times 100, \qquad (2.20)$$

# 3. RESULTS AND DISCUSSION

In this chapter the results obtained for the different case studies mentioned previously are presented and analyzed. The optimal configuration of the RPD is defined and the effect of respiration on the PF is highlighted. A comparison between the different turbulence models is also exhibited.

## 3.1. Optimization of the original prototype

As previously mentioned, for the optimization of the original prototype different sets of jet velocity values and tilt angles of the fourth jet were tested. The results obtained for the different optimization simulations are presented next.

### 3.1.1. Velocity optimizations

The PFs obtained for the velocity sets mentioned earlier on this text are displayed in Table 3.1. Analyzing these results, one immediately concluded that the concept in which the jet velocity sets were based led to higher PFs of the RPD, in most cases.

**Table 3.1.** PFs of the RPD for the different velocity sets.

|  | **RNG Model** | **SST Model** | **BSL Model** |
|---|---|---|---|
| **PF of the 1st set** | 27.0 % | 59.3 % | 61.3 % |
| **PF of the 2nd set** | 48.0 % | 77.4 % | 74.0 % |
| **PF of the 3rd set** | 56.0 % | 83.6 % | 82.9 % |
| **PF of the 4th set** | 92.4 % | 79.3 % | 79.3 % |
| **PF of the 5th set** | 100.0 % | 100.0 % | 100.0 % |
| **PF of the 6th set** | 2.7 % | 75.6 % | 66.2 % |

It is also evident that, when the jet velocities decreased, higher values of protection were achieved. This happened because, as the jet velocities decrease, the momentum of the

air curtain, specially of the frontal jets, also decreases. This, in turn, leads to an earlier separation of the flow from the visor shield, as shown in Figure 3.1 and Figure 3.2, promoting air circulation near the user's face and a dilution of the contaminated air. Such a conclusion shows that a stable air curtain that sticks to the visor shield for a longer distance, in these conditions, does not correspond to higher values of PF. In contrast, the air circulation near the user's face might have negative effects, such as dryness of the mucous membranes.



1ˢᵗ velocity set

2ⁿᵈ velocity set

3ʳᵈ velocity set

4ᵗʰ velocity set

5ᵗʰ velocity set
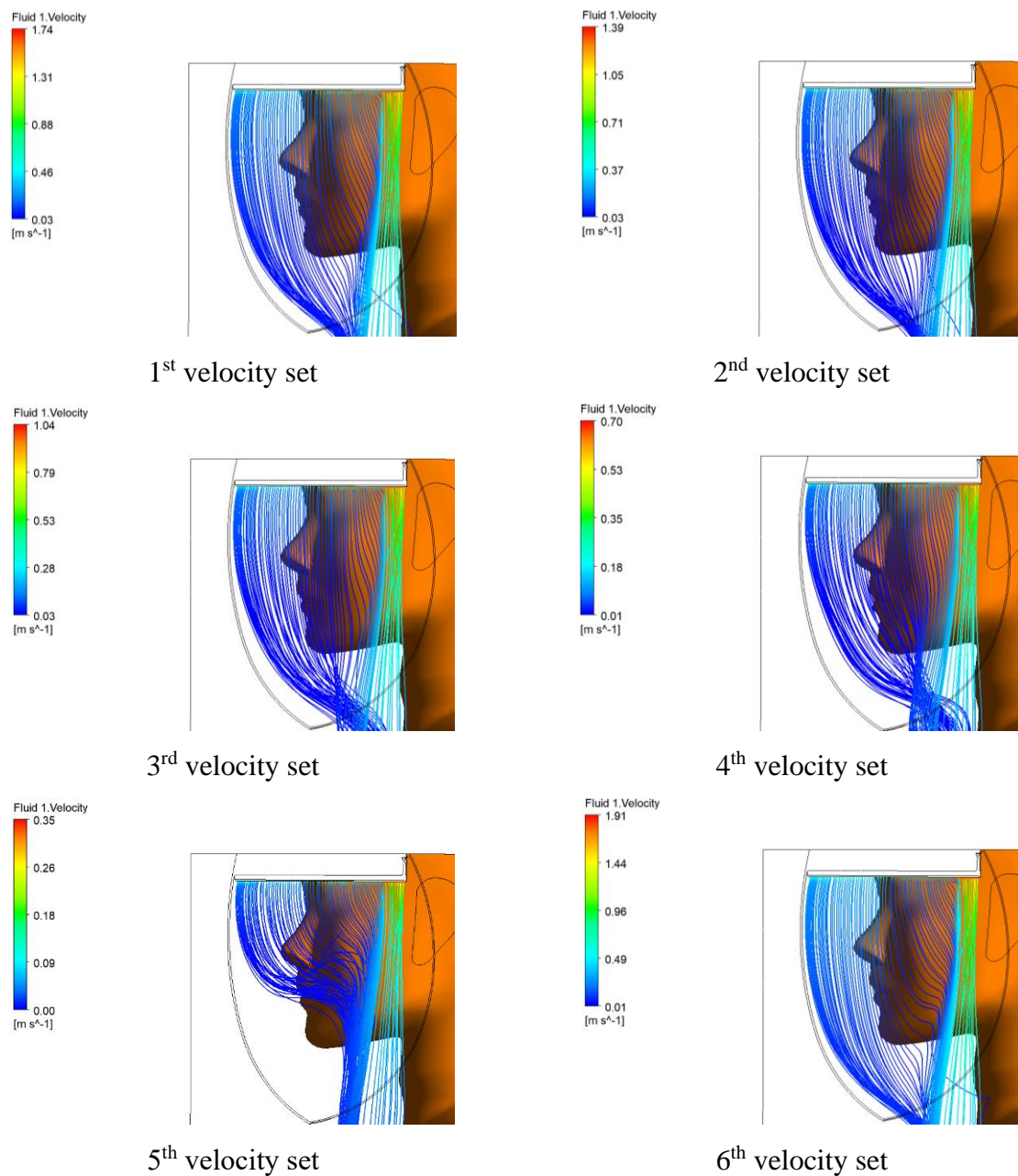
6ᵗʰ velocity set

**Figure 3.1.** Streamlines of the air flow inside the RPD for the different velocity sets (RNG model).

Comparing the results of the three turbulence models, it was noted a significant difference between the values of the RNG model and the other two models, that were similar. This was due to the fact that the RNG model predicted a far more stable air curtain relatively to the other models, as depicted by Figure 3.1 and Figure 3.2, which did not allow an intense mixture between the contaminated air and the cleaned air, and also facilitated the entrance of the first one. The last velocity set offered a good example of this behavior.



1st velocity set



2nd velocity set



3rd velocity set



4th velocity set



5th velocity set
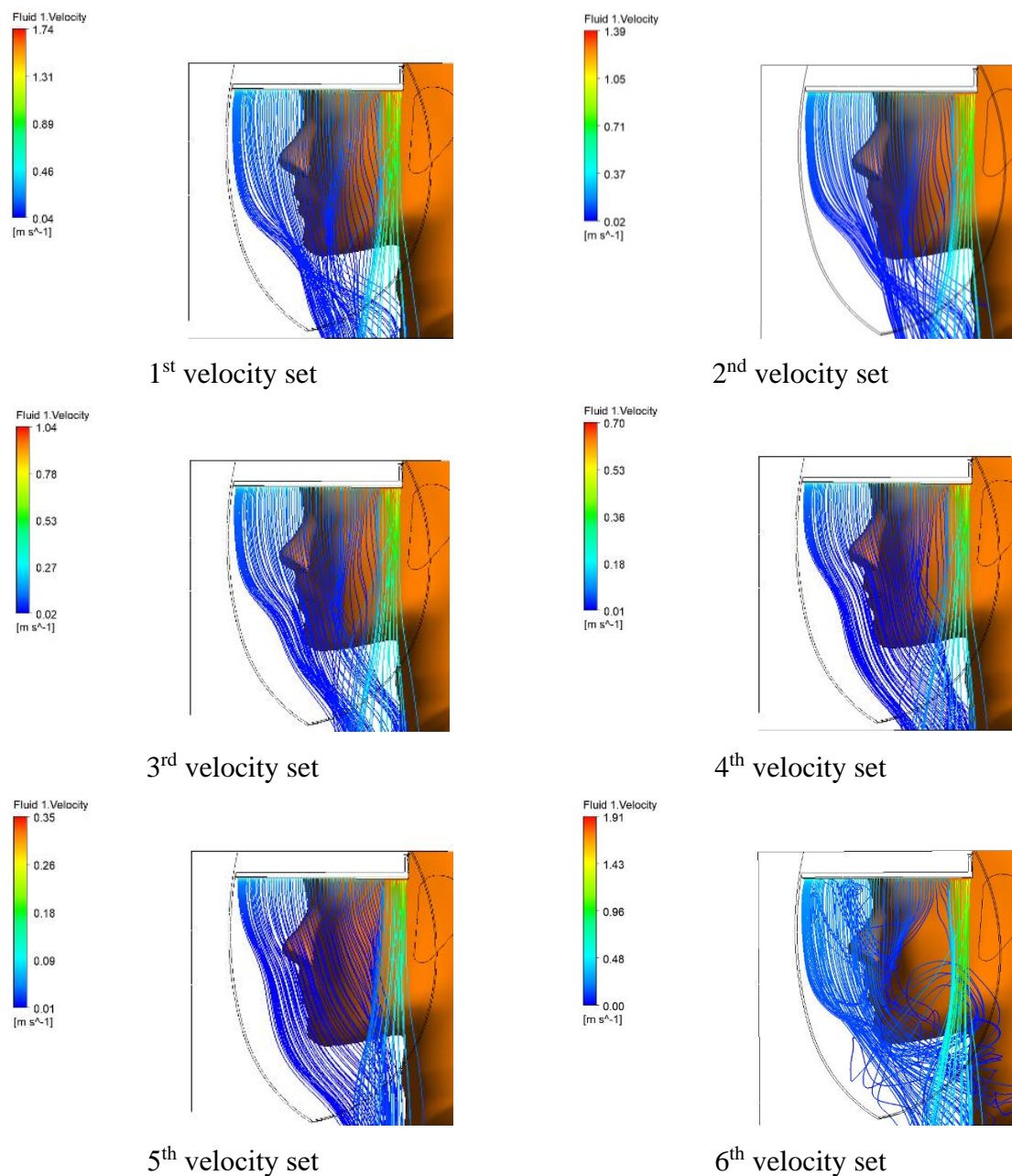


6th velocity set

**Figure 3.2.** Streamlines of the air flow inside the RPD for the different velocity sets (BSL model).

Having what has been said so far in consideration, the two velocity sets chosen for the remaining analysis were the first and fourth ones. The first one was chosen because it had the most beneficial air curtain characteristics, in terms of comfort for the user. The fourth one was chosen because it had the best contaminant distribution in the symmetry plane, as shown in Figure 3.3 for the RNG model.

1st velocity set


2nd velocity set


3rd velocity set


4th velocity set


5th velocity set


6th velocity set

**Figure 3.3.** Contaminant distribution in the symmetry plane for each velocity set (RNG model).

Finally, it is important to mention that these velocity sets, as intended, mitigated the problem associated with the entrainment of the fourth jet.

## 3.1.2. Angle optimizations

The PFs obtained for the angles mentioned earlier on this text are displayed in Figure 3.4 and Figure 3.5, for the first and fourth velocity sets, respectively.

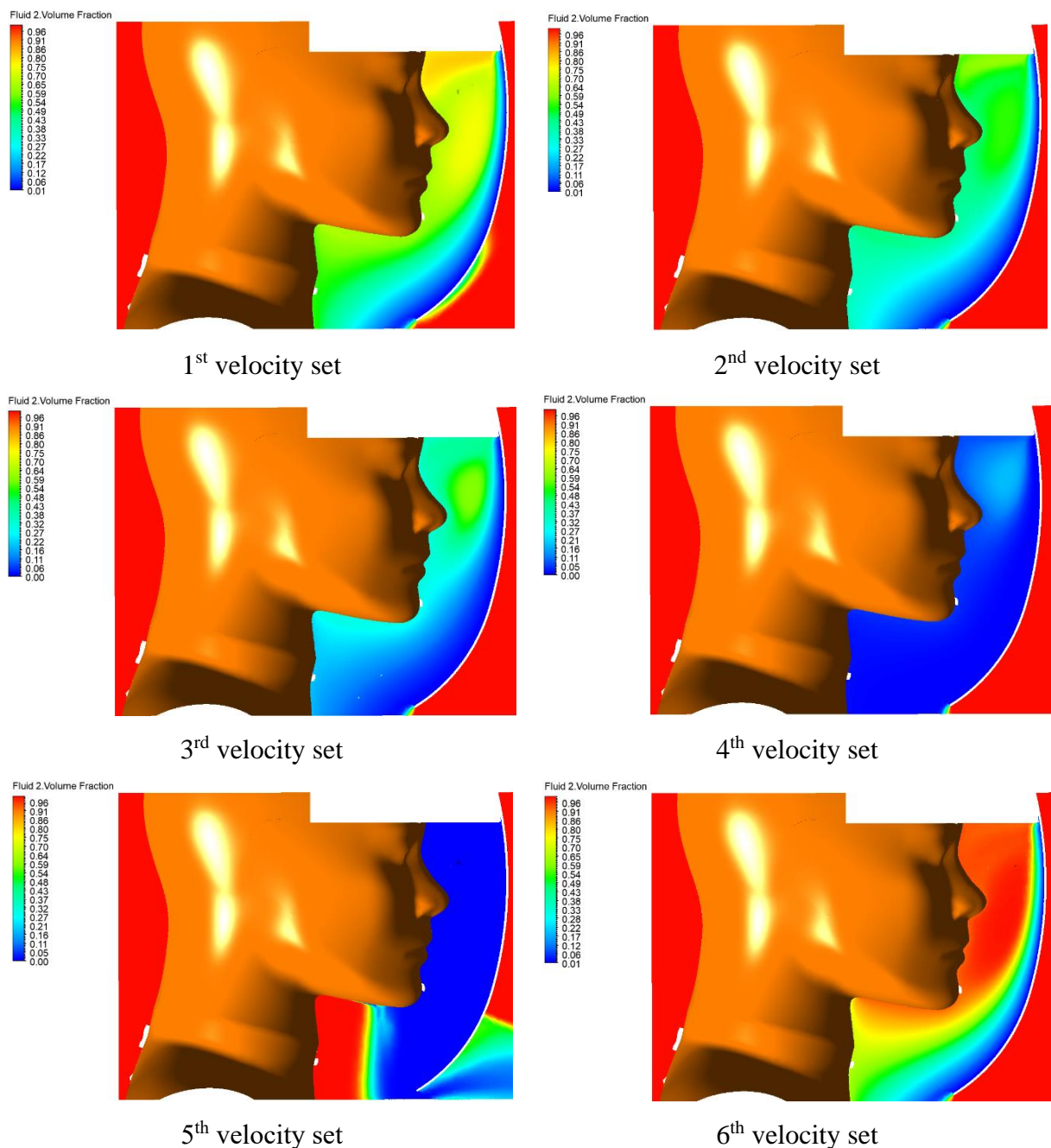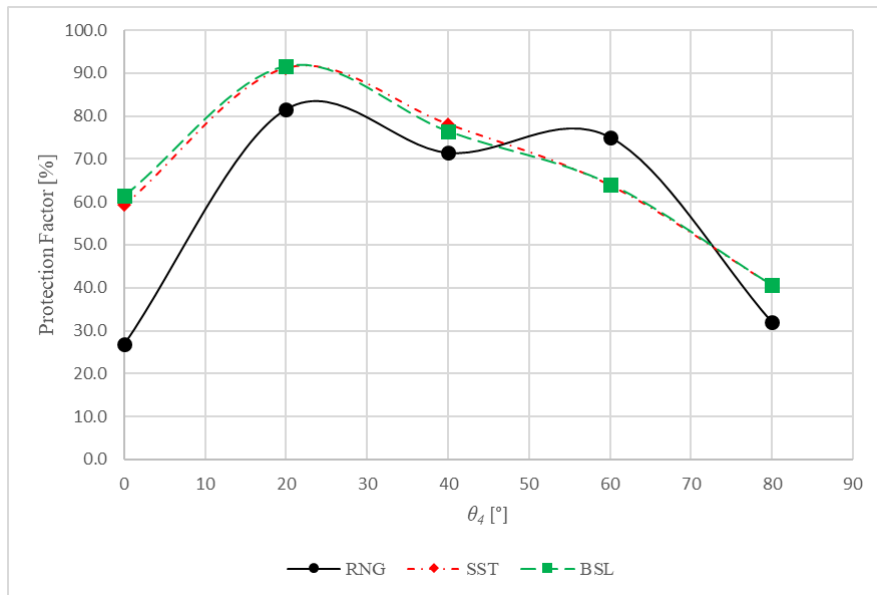**Figure 3.4.** Protection factor variation with the tilt angle of the 4<sup>th</sup> jet for the 1<sup>st</sup> velocity set.
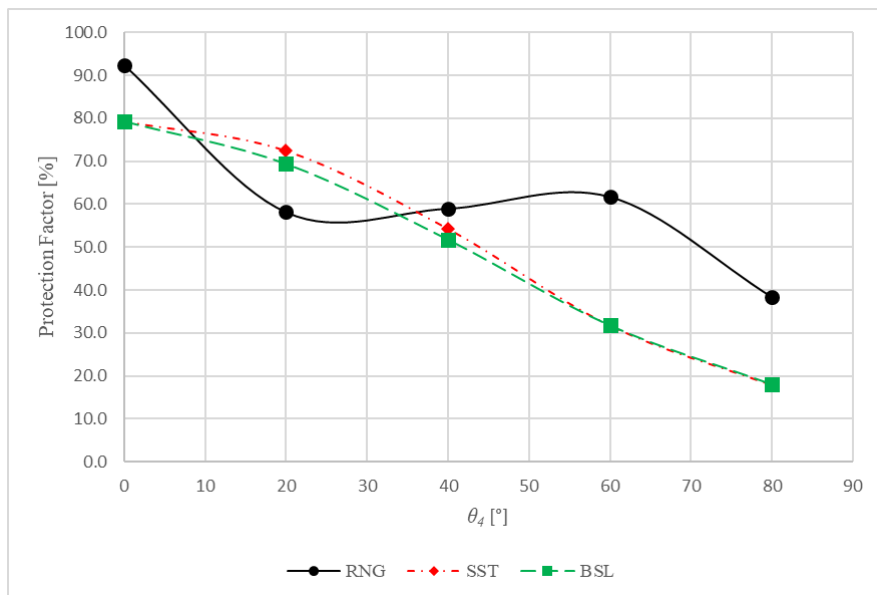


**Figure 3.5.** Protection factor variation with the tilt angle of the 4<sup>th</sup> jet for the 4<sup>th</sup> velocity set.

Analyzing Figure 3.4, one could conclude that, for the first velocity set, the optimal tilt angle of the fourth jet was 20°. This angle allowed the sealing of the space between the user's face and the visor, through which contaminated air could easily enter, as can be seen in Figure 3.6. For higher values of this angle the air coming out of the fourth jet started to

get entrained into the visor's interior, which led to lower PFs. There was an exception for the RNG model for the value of $60°$. In the case of $\theta_4 = 0°$, the sealing of the breathing zone was not enough, even though the suction of the fourth's jet air was very small.



$$\theta_4 = 20°$$

$$\theta_4 = 40°$$

$$\theta_4 = 60°$$

$$\theta_4 = 80°$$
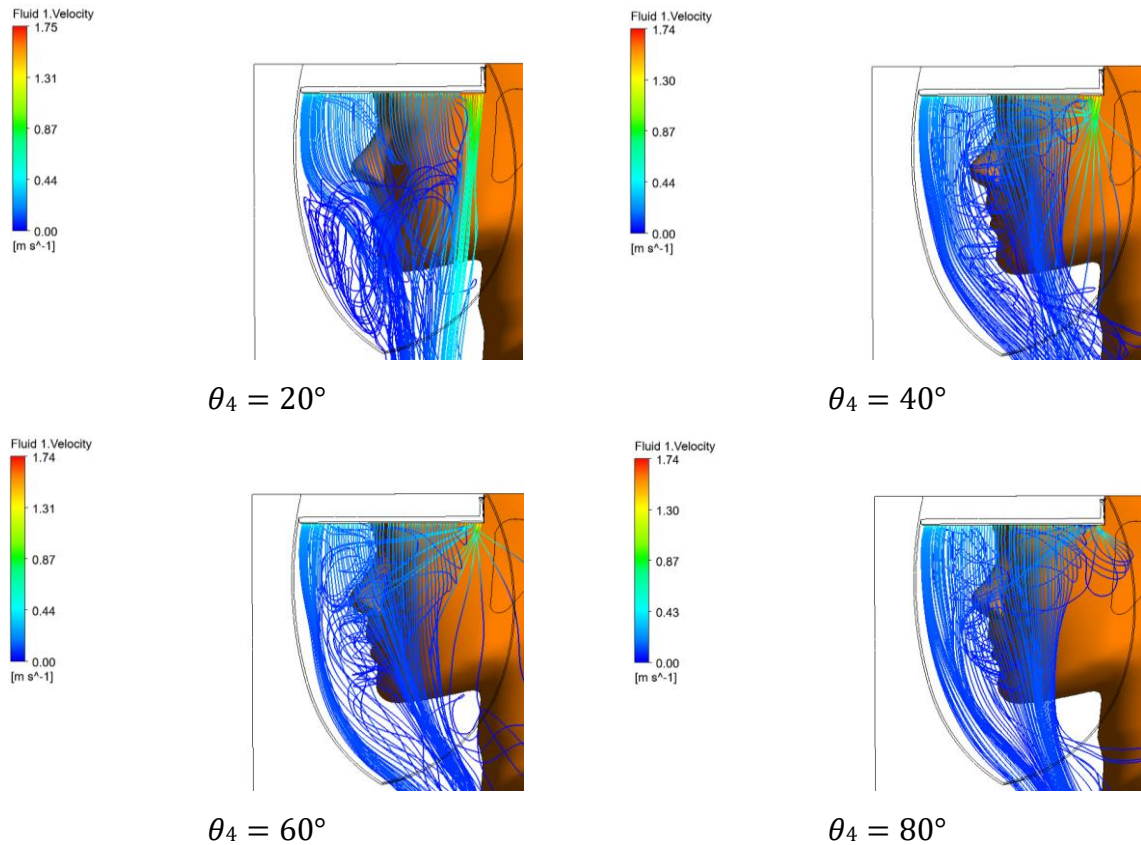
**Figure 3.6.** Streamlines of the air flow inside the RPD for each value of $\theta_4$ (SST model and 1st velocity set).

Examining Figure 3.5, it was possible to understand that for the fourth velocity set, the optimal tilt angle of the fourth jet was $0°$. Higher values of this angle led to a high entrainment of the fourth's jet air and, therefore, low values of the PF. It is also important to mention that, for this velocity set, the air curtain presented far less vortices, especially in the breathing zone, which is also responsible for lower PFs when compared to the first velocity set (Figure 3.7).

$$\theta_4 = 20°$$ $$\theta_4 = 40°$$

$$\theta_4 = 60°$$ $$\theta_4 = 80°$$
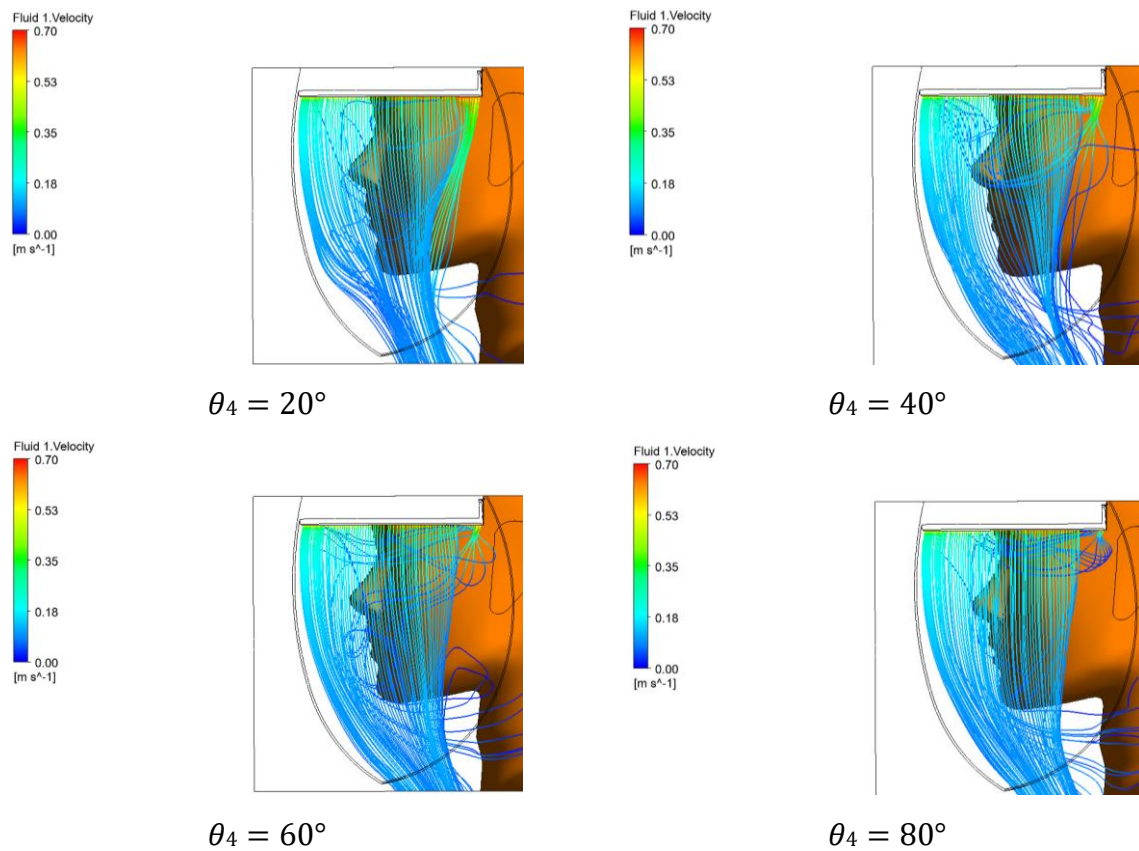
**Figure 3.7.** Streamlines of the air flow inside the RPD for each value of $\theta_4$ (SST model and 4th velocity set).

Once again, the results for the RNG model were quite different from the ones obtained for the SST and BSL models.

## 3.2. Original prototype with respiration

The PFs for the cases with the breathing process and without it obtained for the original prototype, for each turbulence model, are presented in Table 3.2. The results for the SST and BSL models were identical, as well as their behavior. The contaminant fraction evolution in the symmetry plane, for the RNG and the SST models, are presented in Figure 3.8 and Figure 3.9, respectively. The streamlines evolution for the same models is presented in Figure 3.10 and Figure 3.11, respectively.

**Table 3.2.** PFs of the original prototype with breathing and without breathing.

|  | RNG Model | SST Model | BSL Model |
|---|---|---|---|
| **PF with breathing** | 44.6 % | 49.6 % | 49.7 % |
| **PF without breathing** | 68.2 % | 45.5 % | 45.5 % |

Analyzing the PFs and the contaminant fraction evolutions, one concludes that the performance of the RNG model drops, as expected, while the performance of the other two models is enhanced. The key to understanding this phenomenon lies in understanding how breathing affects the air curtain.

For the first model, on examining the streamlines evolution mentioned before, it can be seen that the expiration process broke the air curtain and that the inspiration process promoted the aspiration of the air from the fourth and third jets with little disturbance from the air around the breathing zone. Both of these factors led to a decrease in the sealing efficiency of the air curtain. It is also interesting to notice that the expiration promoted the cleaning of the respiration zone while the inspiration helped the entrainment of contaminated air.
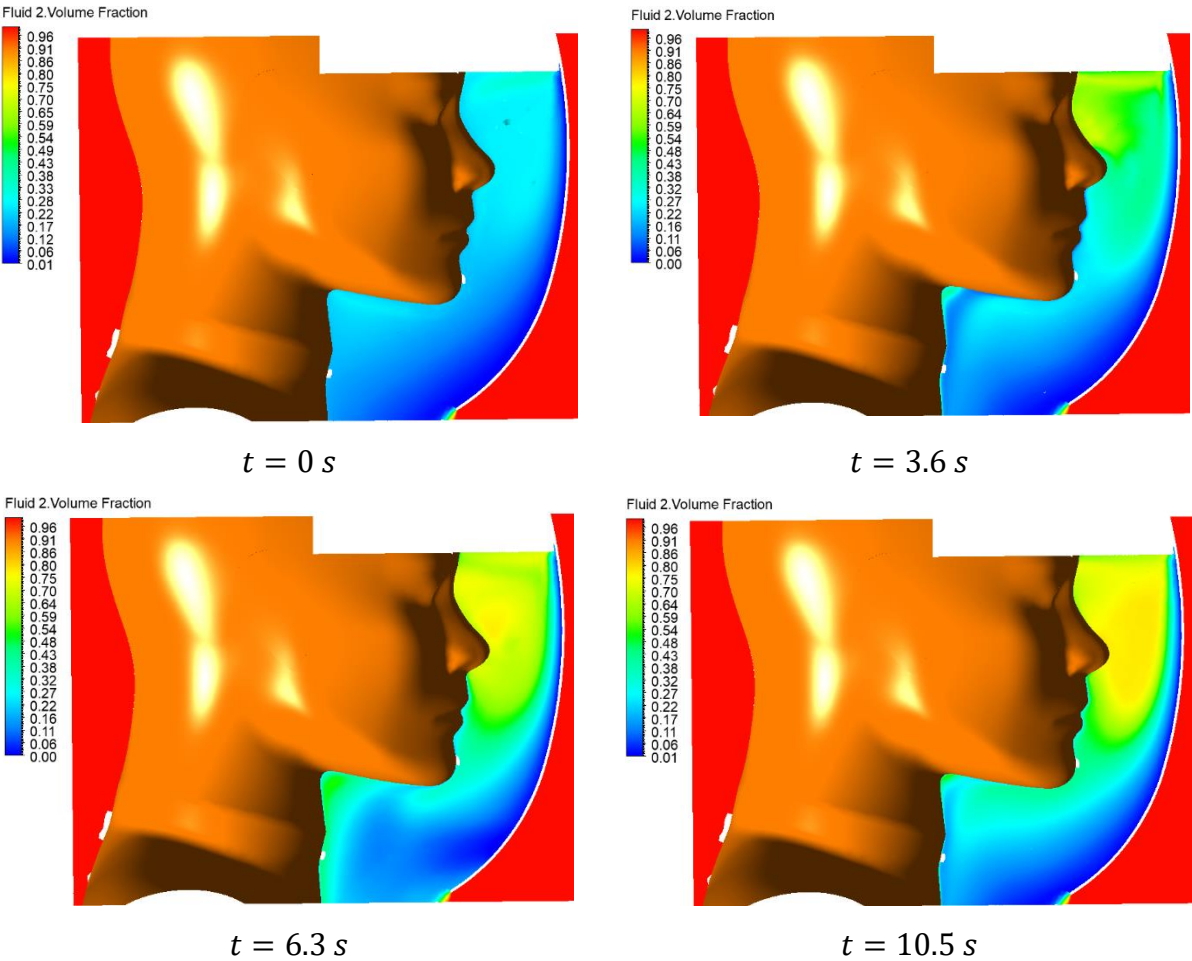
$$t = 0\ s \qquad\qquad t = 3.6\ s$$

$$t = 6.3\ s \qquad\qquad t = 10.5\ s$$

**Figure 3.8.** Evolution of the contaminant distribution in the symmetry plane (RNG model).

$t = 0\ s$

$t = 3.6\ s$

$t = 6.3\ s$

$t = 10.5\ s$
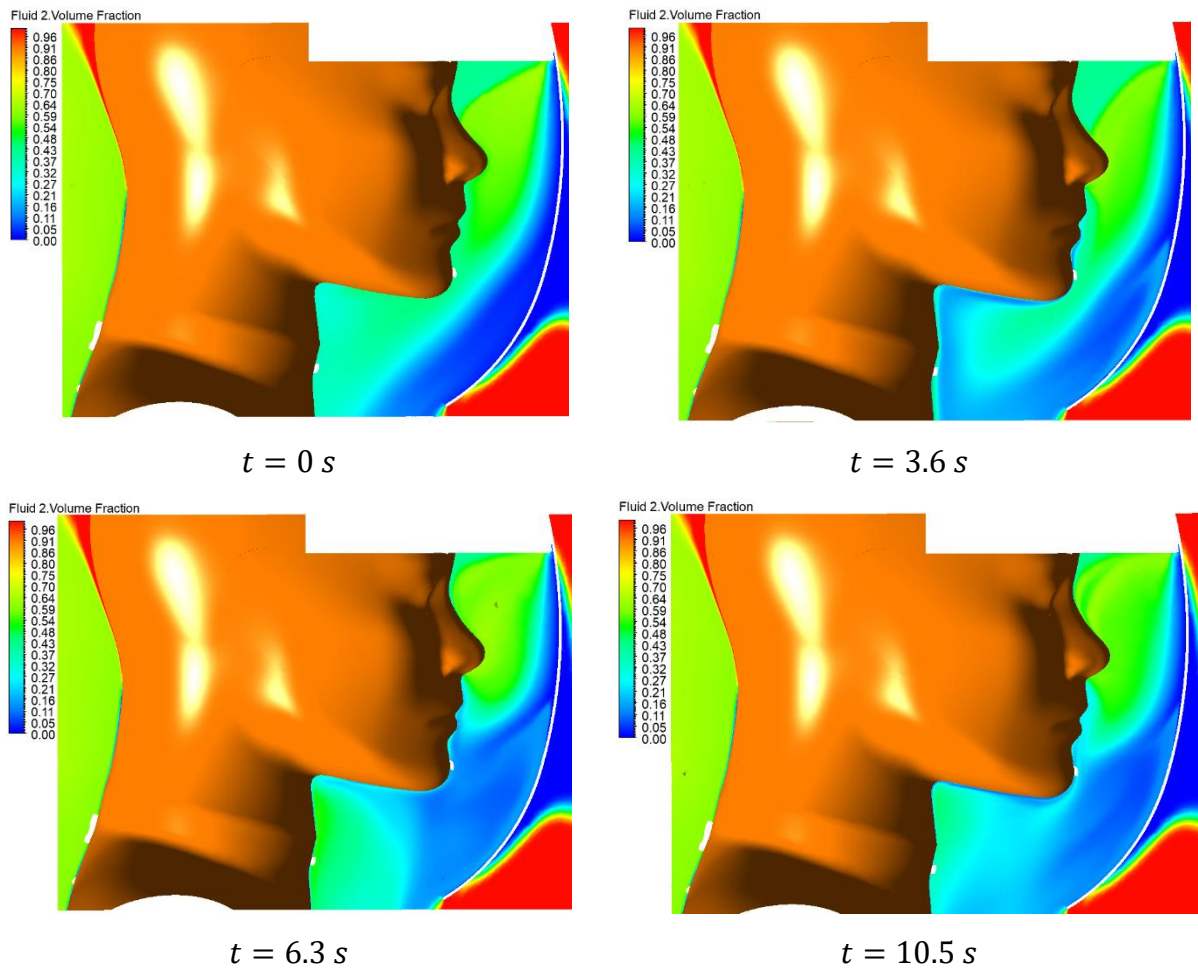
**Figure 3.9.** Evolution of the contaminant distribution in the symmetry plane (SST model).

The other two models predicted far more vortices inside the RPD and a less stable air curtain when compared with the first model. A higher number of vortices and an air curtain closer to the user's face promoted a greater mixture of contaminated air with cleaned air inside the RPD, which in turn diluted the fraction of the first one, giving the SST and the BSL models a better performance regarding respiration, and a better performance when compared with the case without respiration.

It is also important to note that for the RNG model, the PF drops significantly when breathing is introduced because in the case of no respiration, this model predicted an air curtain far more stable than the other models which corresponded to less entrainment of the air coming out the fourth jet.

$t = 0\ s$        $t = 0\ s$

$t = 0.9\ s$        $t = 0.9\ s$

$t = 2.7\ s$        $t = 2.7\ s$

$t = 3.6\ s$        $t = 3.6\ s$

a)        b)

**Figure 3.10.** Evolution of the flow streamlines (RNG model): a) side view; b) front view.

$t = 0\ s$        $t = 0\ s$

$t = 0.9\ s$        $t = 0.9\ s$

$t = 2.7\ s$        $t = 2.7\ s$

$t = 3.6\ s$        $t = 3.6\ s$

a)        b)

**Figure 3.11.** Evolution of the flow streamlines (SST model): a) side view; b) front view.

## 3.3. Optimized version with respiration

Two optimized configurations of the RPD were tested with respiration, the configuration with the first velocity set and $\theta_4 = 20°$ and the configuration with the fourth velocity set and $\theta_4 = 0°$. These were chosen because they had the best performance out of all the optimization simulations. The BSL and SST models had, once again, similar results.

The PFs with the breathing process implemented, and without it, obtained for the first optimized version of the RPD mentioned earlier, for each turbulence model, are presented in Table 3.3. The streamlines evolution for the RNG and SST models is presented in Figure 3.12 and Figure 3.13, respectively.

**Table 3.3.** PFs of the optimized prototype ($1^{st}$ velocity set and $\theta_4 = 20°$), with breathing and without breathing.

|                          | RNG Model | SST Model | BSL Model |
| ------------------------ | --------- | --------- | --------- |
| **PF with breathing**    | 84.0 %    | 90.6 %    | 90.8 %    |
| **PF without breathing** | 81.5 %    | 91.2 %    | 91.5 %    |

Contrary to what happened in the second case study, this time the performance of the RNG model was enhanced by the respiration process, while the performance of the other models was not. It is important to note, though, that the decrease of the PF in the SST and BSL models was so small that can be neglected. For this configuration of the RPD, the air coming out of the fourth jet was practically undisturbed, which allowed a very high sealing efficiency of the visor. For the RNG model, this fact combined with a higher recirculation rate inside the RPD promoted by the respiration, led to a better performance.

It is also important to mention that the mass flux of air of this configuration was approximately 27% higher than the mass flux of the original prototype, which leads to more noise and a higher consumption of energy.
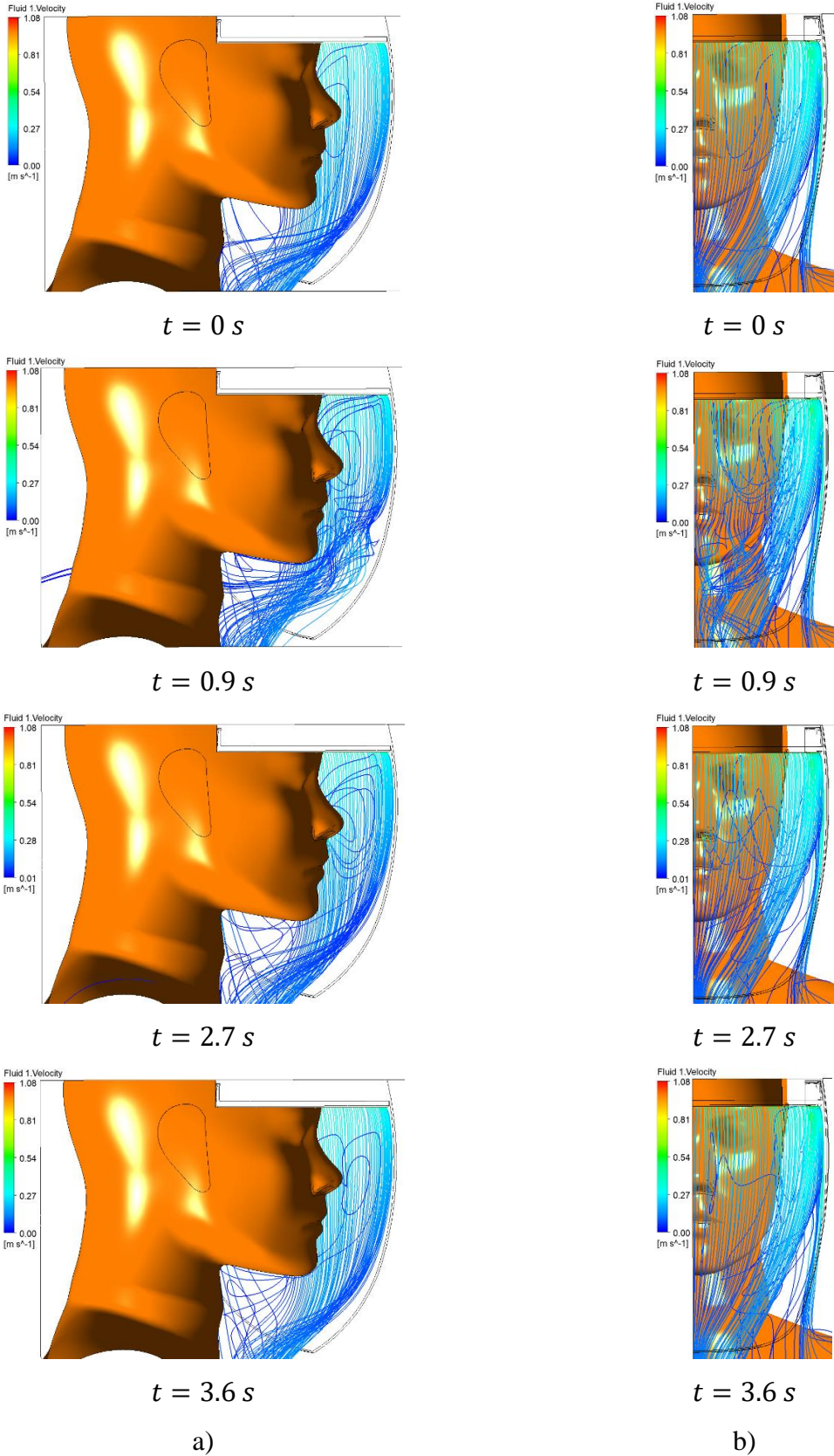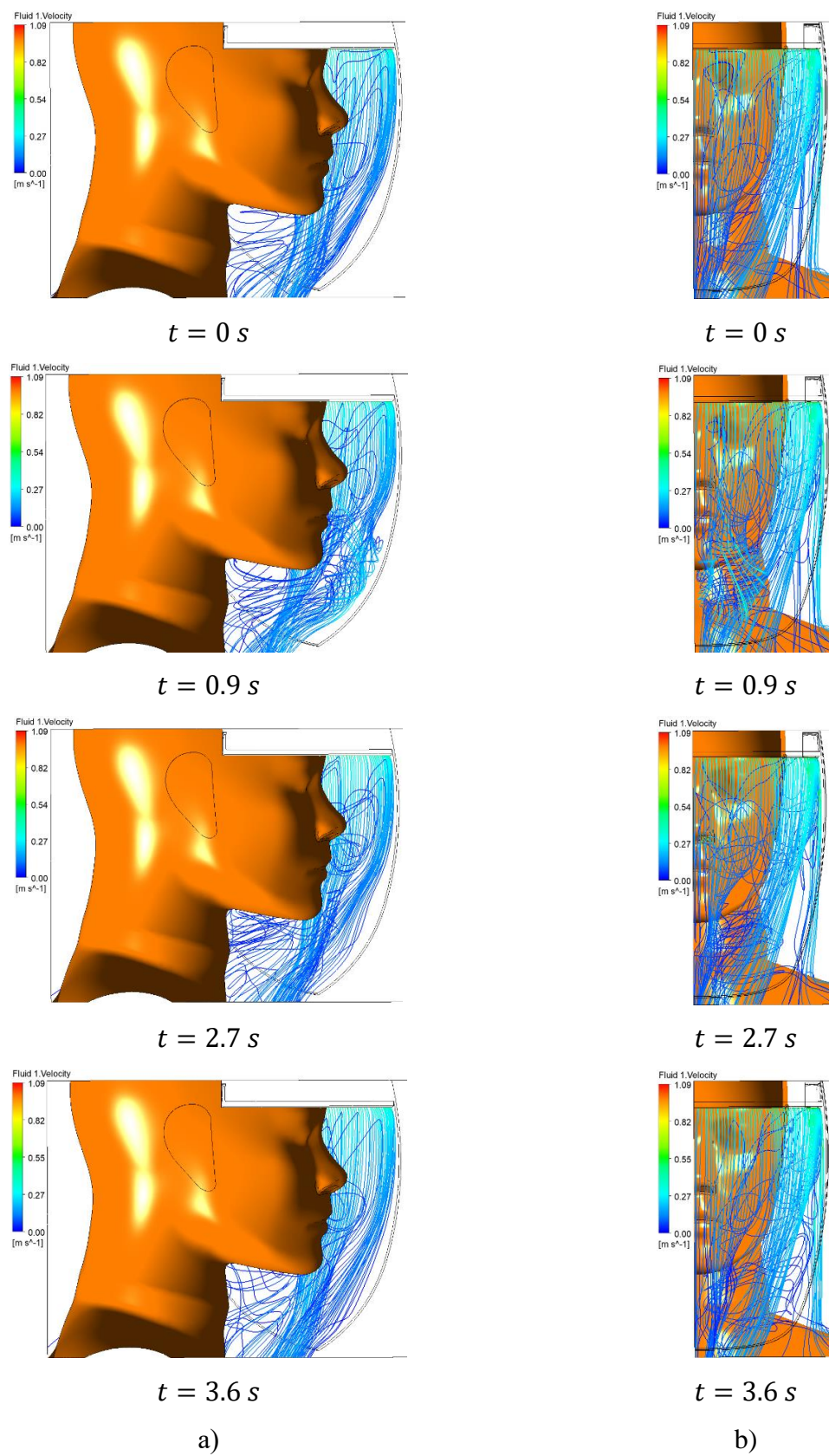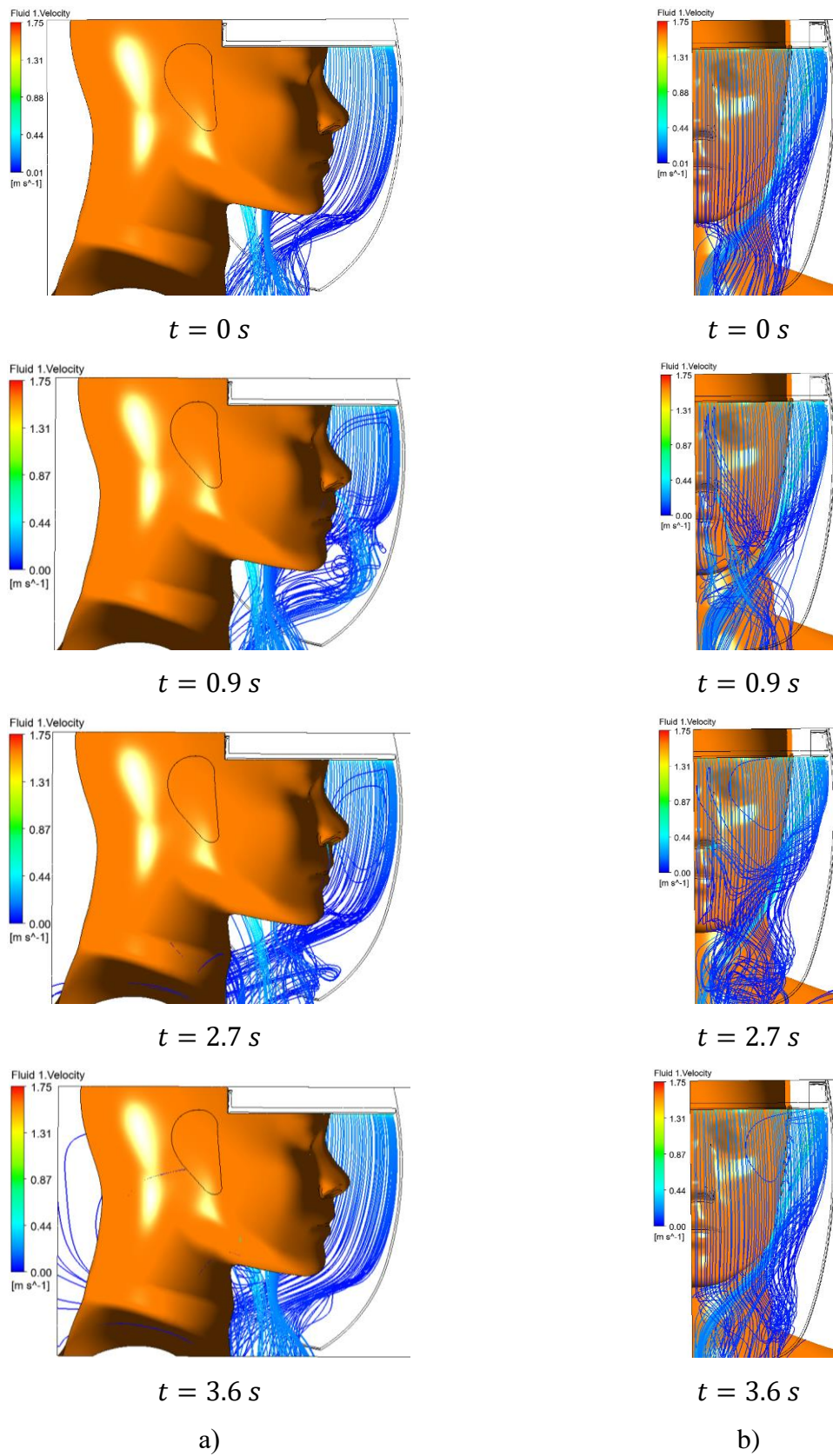
Figure 3.12. Evolution of the flow streamlines (RNG model, 1st velocity set): a) side view; b) front view.
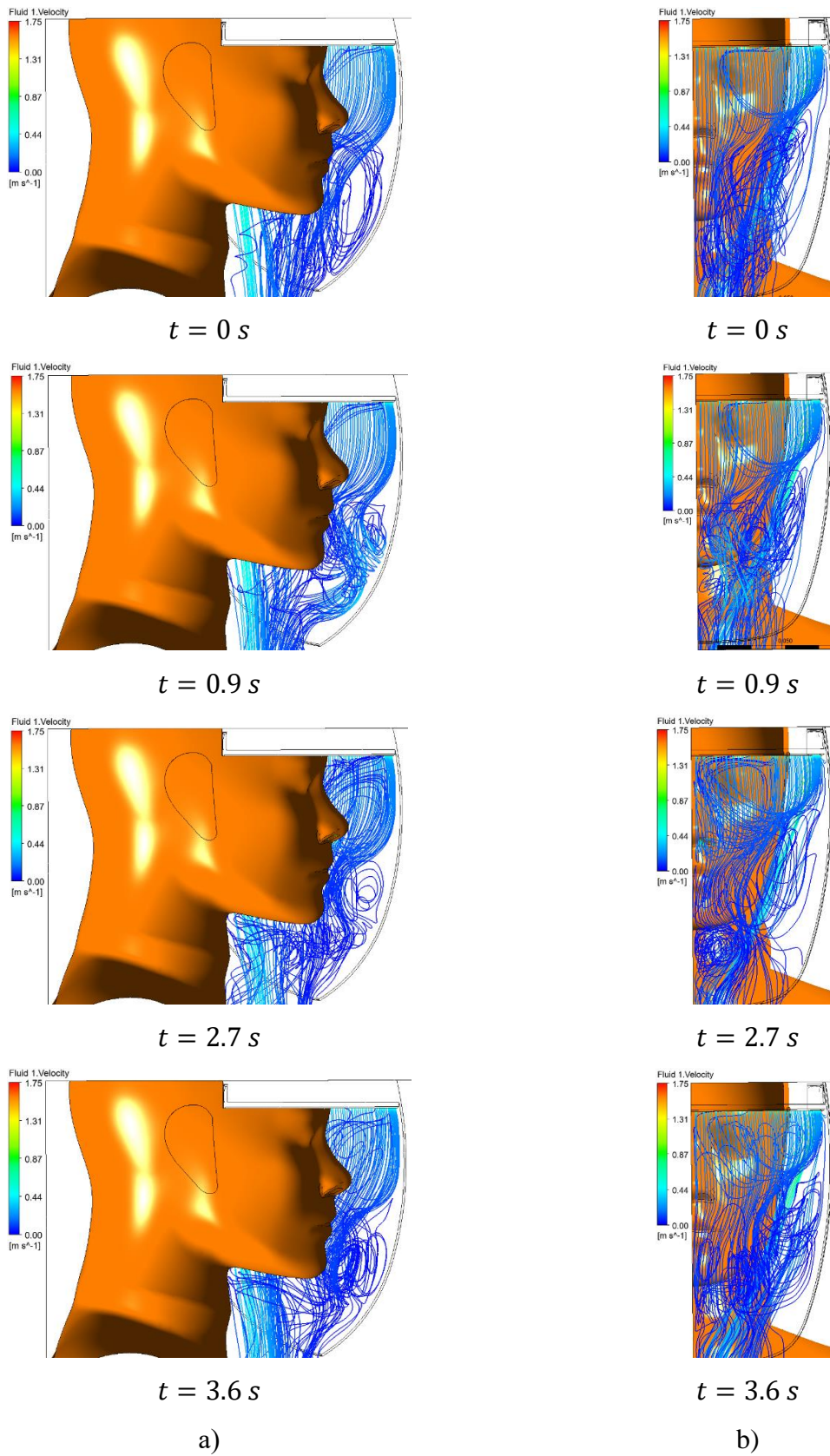
Figure 3.13. Evolution of the flow streamlines (SST model, 1st velocity set): a) side view; b) front view.

The PFs with the breathing process implemented, and without it, obtained for the second optimized version of the RPD mentioned earlier, for each turbulence model, are presented in Table 3.4. The streamlines evolution for the RNG and SST models is presented in Figure 3.14 and Figure 3.15, respectively.

**Table 3.4.** PFs of the optimized prototype (4th velocity set), with breathing and without breathing.

|  | **RNG Model** | **SST Model** | **BSL Model** |
|---|---|---|---|
| **PF with breathing** | 91.1 % | 75.6 % | 75.4 % |
| **PF without breathing** | 92.4 % | 79.3 % | 79.3 % |

This time, the introduction of respiration led to a decrease of the PF in all models, especially in the SST and BSL models. This was due to the fact that the air curtain of this configuration had lower momentum when compared with the last one, making it a lot more fragile. It is also worth mentioning that in this case there was fewer vortices near the mannequin's eyes, which increases the user's comfort.

The mass flux of air of this configuration was half of the original mass flux, leading to less energy consumption and less noise.
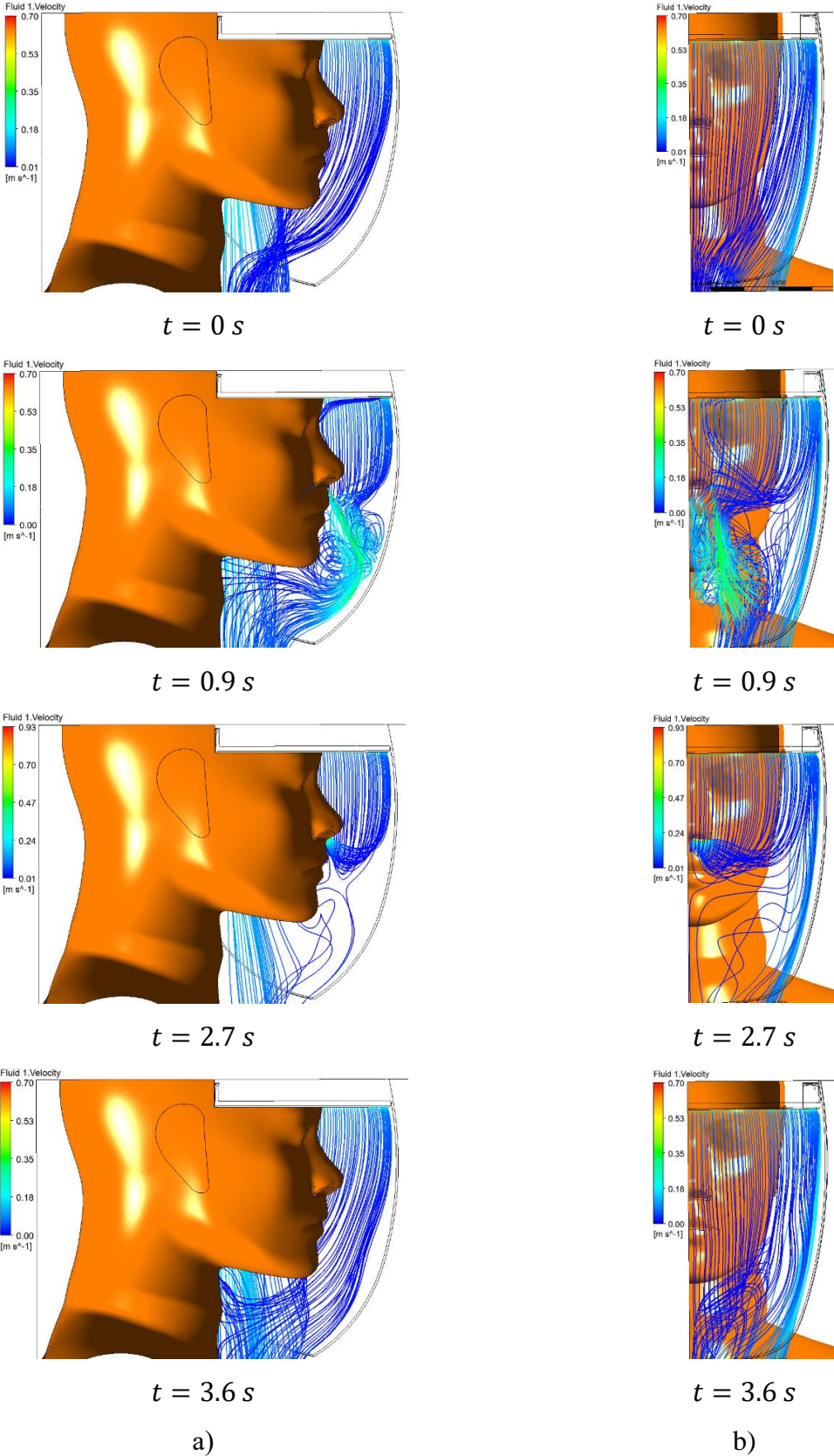
**Figure 3.14.** Evolution of the flow streamlines (RNG model, 4th velocity set): a) side view; b) front view.
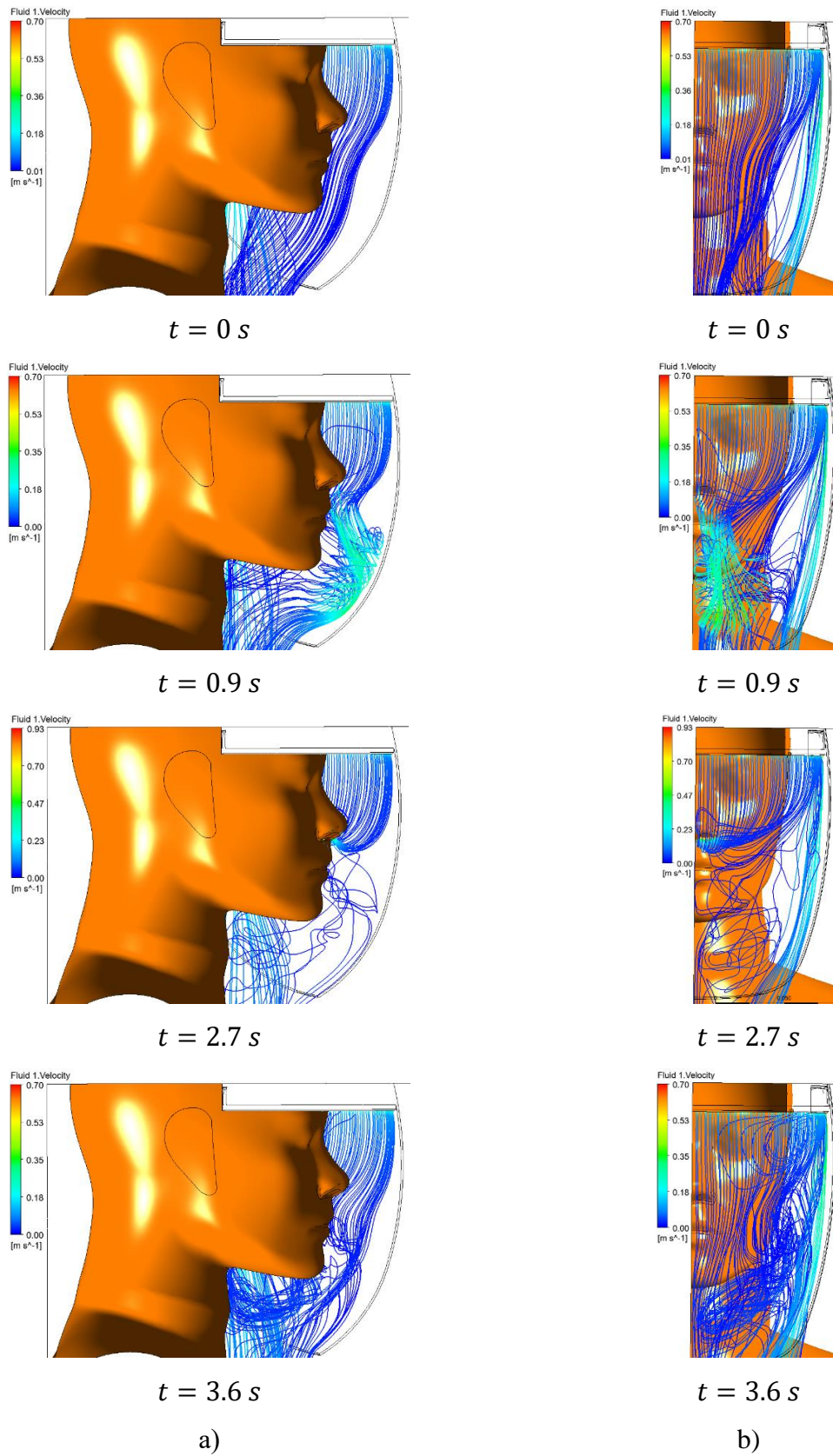
**Figure 3.15.** Evolution of the flow streamlines (SST model, 4th velocity set): a) side view; b) front view.

## 3.4. Turbulence model performance

Based on what has been said so far, one could conclude that the results given by the RNG model were quite different from the ones given by the other models. The SST and BSL models had a very similar performance. The usage of different types of wall treatment also promoted a discrepancy between the models.

The air flow predicted by the RNG model presented fewer vortices and an air curtain more stable and uniform, when compared with the other models. The RNG model also predicted a later separation of the flow from the visor shield.

Is also worthy of note that, even though the performance of all three models was higher for lower velocities, the results computed with the RNG model for higher velocities were far worse than the ones obtained by the other models. The behavior of all models regarding the variation of the tilt angle of the fourth jet was, in general, similar, but with different results.

The introduction of breathing in the original prototype led to close results for all models. This fact was not observed in the case of the optimized versions with respiration.

# 4. CONCLUSIONS

In this work, an optimization study of the MASK4MC prototype was carried out in order to improve its PF and solve the suction of the air coming out of the fourth jet. Then the behavior of the original and the optimized version of the prototype with the user's respiration implemented was studied. Three different turbulence models were used in order to compare the results obtained by each model.

Regarding the optimization of the prototype, firstly different sets of velocities were simulated. The aim of these simulations was to study the effect of the jet velocities on the PF and to solve the suction problem associated with the fourth jet by making the momentum of this jet equal to the sum of the momentum of the other jets. The results of these simulations showed not only that the PF rises as the jet velocities decrease but also that this approach eliminated the suction of the fourth jet. One other conclusion withdrawn from these tests was that the PFs of the BSL and SST models were, generally, higher than the ones of the RNG model.

After these simulations, different tilt angles of the fourth jet (between the values of $0°$ and $80°$, with an increment of $20°$) were tested for two of the velocity's sets mentioned, the first and fourth ones. For the first velocity set ($V_4 = 1.74 \, m/s$) the maximum value of PF was obtained for an angle equal to $20°$ and the RPD also had a good performance for a tilt angle of $40°$. For the second velocity set ($V_4 = 0.7 \, m/s$) the maximum value of PF was obtained for an angle equal to $0°$, with a significant performance drop for the other angles.

The influence of the user's respiration was then tested both on the original prototype and in these last two optimized configurations. In the first case, the RNG model predicted a performance drop of the RPD (the PF decreased 23.6 %), while the other turbulence models projected a slight enhancement of the performance (the PF increased 4.1 % and 4.2 % for the SST and BSL models, respectively). In the second case, the breathing process had little effect on the PF. From these simulations it was also possible to conclude that the expiration process promoted the cleaning of the breathing zone, while the inspiration process aided the entrance of polluted air.

Of the two optimized configurations of the RPD, the better one was the second, because it combined an air curtain that provided high values of PF across all turbulence

models (the PF increased, relatively to the original prototype, 24.1 % for the RNG model and 33.8 % for the SST and BSL models) and a stable air curtain without recirculation zones near the user's nose or eyes. When compared with the original prototype, this configuration used half of the mass flux, leading to less energy consumption and less noise.

Analyzing the results obtained by each turbulence model was possible to conclude that the RNG model predicted values of PF, in practically all case studies, that were quite different from the ones determined by the SST and BSL models. The air curtain of the RNG model presented fewer vortices and was more stable and uniform, when compared with the other models. This turbulence model also predicted a later separation of the flow from the visor shield.

Other simulations are of interest to optimize the RPD, in particular the variation of the outlet width of the fourth jet. The development of a plenum that allows the optimal configuration mentioned earlier should also be the aim of future work. Finally, an experimental validation of the numerical simulations here presented would be of the most importance.

# REFERENCES

Ansys CFX-Solver Modeling Guide. (2022). http://www.ansys.com

Ansys CFX-Solver Theory Guide. (2022). http://www.ansys.com

Consórcio MASK4MC Instituição. (2021). 2º RELATÓRIO TÉCNICO.

Gao, N., & Niu, J. (2006). Transient CFD simulation of the respiration process and inter-person exposure assessment. Building and Environment, 41(9), 1214–1222. https://doi.org/10.1016/J.BUILDENV.2005.05.014.

L. A. Oliveira, & A. G. Lopes. (2016). Mecânica dos Fluidos (5th ed.). LIDEL – Edições Técnicas.

Moureh, J., & Yataghene, M. (2016). Numerical and experimental investigations on jet characteristics and airflow patterns related to an air curtain subjected to external lateral flow. International Journal of Refrigeration, 67, 355–372. https://doi.org/10.1016/J.IJREFRIG.2016.03.002.

Versteeg, H. K., & Malalasekera, W. (2007). An Introduction to Computational Fluid Dynamics (2nd ed.). Pearson Education.

Wei, X., Yi, D., Xie, W., Gao, J., & Lv, L. (2021). Protection against inhalation of gaseous contaminants in industrial environments by a personalized air curtain. Building and Environment, 206, 108343. https://doi.org/10.1016/J.BUILDENV.2021.108343